Lawrence Berkeley National Laboratory
Recent Work

Title
RADIO OBSERVATIONS of A SAMPLE of BROAD-LINE TYPE IC SUPERNOVAE DISCOVERED by PTF/IPTF: A SEARCH for RELATIVISTIC EXPLOSIONS

Permalink
https://escholarship.org/uc/item/7x9964b4

Journal
Astrophysical Journal, 830(1)

ISSN
0004-637X

Authors
Corsi, A
Gal-Yam, A
Kulkarni, SR
et al.

Publication Date
2016-10-10

DOI
10.3847/0004-637X/830/1/42

Peer reviewed

RADIO OBSERVATIONS OF A SAMPLE OF BROAD-LINED TYPE IC SUPERNOVAE DISCOVERED BY PTF/IPTF: A SEARCH FOR RELATIVISTIC EXPLOSIONS

A. Corsi[1], A. Gal-Yam[2], S. R. Kulkarni[3], D. A. Frail[4], P. A. Mazzali[5,6], S. B. Cenko[7,8], M. M. Kasliwal[3],
Y. Cao[3], A. Horesh[2], N. Palliyaguru[1], D. A. Perley[9], R. R. Laher[10], F. Taddia[11], G. Leloudas[2,9], K. Maguire[12],
P. E. Nugent[13,14], J. Sollerman[11], M. Sullivan[15]

November 1, 2016

ABSTRACT

Long duration γ-ray bursts are a rare subclass of stripped-envelope core-collapse supernovae that launch collimated relativistic outflows (jets). All γ-ray-burst-associated supernovae are spectroscopically of Type Ic with broad lines, but the fraction of broad-lined Type Ic supernovae harboring low-luminosity γ-ray-burst remains largely unconstrained. Some supernovae should be accompanied by off-axis γ-ray burst jets that remain invisible initially, but then emerge as strong radio sources (as the jets decelerate). However, this critical prediction of the jet model for γ-ray bursts has yet to be verified observationally. Here, we present K. G. Jansky Very Large Array observations of 15 broad-lined supernovae of Type Ic discovered by the Palomar Transient Factory in an untargeted manner. Most of the supernovae in our sample exclude radio emission observationally similar to that of the radio-loud, relativistic SN 1998bw. We constrain the fraction of 1998bw-like broad-lined Type Ic supernovae to be $\lesssim 41\%$ (99.865% confidence). Most of the events in our sample also exclude off-axis jets similar to GRB 031203 and GRB 030329, but we cannot rule out off-axis γ-ray-bursts expanding in a low-density wind environment. Three supernovae in our sample are detected in the radio. PTF11qcj and PTF14dby show late-time radio emission with average ejecta speeds of $\approx 0.3 - 0.4\,c$, on the dividing line between relativistic and "ordinary" supernovae. The speed of PTF11cmh radio ejecta is poorly constrained. We estimate that $\lesssim 85\%$ (99.865% confidence) of the broad-lined Type Ic supernovae in our sample may harbor off-axis γ-ray-bursts expanding in media with densities in the range probed by this study.

Subject headings: gamma-ray burst: general — radiation mechanisms: non-thermal — supernovae: general

1. INTRODUCTION

Long-duration ($T_\gamma \gtrsim 2\,\mathrm{s}$) γ-ray bursts (GRBs) are extremely energetic explosions (typically, $\approx 10^{52}$ erg re-leased in $\approx 10\,\mathrm{s}$, also referred to as collapsars) marking the deaths of massive stars (Galama et al. 1998; Woosley & Bloom 2006). According to the popular fireball model (Piran 2004; Mészáros 2006), the explosion launches relativistic jets in which magnetic fields are amplified and particles accelerated (Rhoads 1999). Observers located within the initial jets' opening angle ($\theta_j \gtrsim \theta_{obs}$; "on-axis" observers) see an intense flash of γ-rays. Subsequent emission from the decelerating jets produces a (slowly) decaying broad-band afterglow. If the fireball model is correct, then off-axis GRBs should exist and be $\approx 2/\theta_j^2$ times more common than the ones we see in γ-rays (Granot et al. 2002). While γ-ray emission from off-axis GRBs cannot be observed, their longer-wavelength afterglow emission is expected to become observable at later times, once the jet decelerates and starts spreading (Nakar et al. 2002).

Off-axis GRBs have not been discovered so far, but in the light of the well-established connection between long-duration GRBs and core-collapse supernovae (SNe) of spectral type Ic with broad-lines (BL-Ic; Woosley & Bloom 2006), a natural way to search for off-axis events is to observe this type of SNe and wait for the decelerating jet to emerge. While the SN optical emission traces the slower explosion debris ($v \approx 0.03 - 0.1\,c$), synchrotron emission from the fastest ejecta peaks in the radio band. There can be two major sources of radio emission associated with GRB-SNe,

(i): the SN shock, whose radio emission is brighter and earlier-peaking the faster the SN ejecta,

[1] Department of Physics, Texas Tech University, Box 41051, Lubbock, TX 79409-1051, USA. E-mail: alessandra.corsi@ttu.edu
[2] Benoziyo Center for Astrophysics, Weizmann Institute of Science, 76100 Rehovot, Israel.
[3] Division of Physics, Mathematics, and Astronomy, California Institute of Technology, Pasadena, CA 91125, USA.
[4] National Radio Astronomy Observatory, P.O. Box O, Socorro, NM 87801, USA
[5] Astrophysics Research Institute, Liverpool John Moores University, Liverpool L3 5RF, UK.
[6] Max-Planck Institut fur Astrophysik, Karl-Schwarzschildstr. 1, D-85748 Garching, Germany.
[7] Astrophysics Science Division, NASA Goddard Space Flight Center, Mail Code 661, Greenbelt, MD 20771, USA.
[8] Joint Space-Science Institute, University of Maryland, College Park, MD 20742, USA.
[9] Dark Cosmology Centre, Niels Bohr Institute, University of Copenhagen, Juliane Maries Vej 30, 2100 Copenhagen, Denmark.
[10] Spitzer Science Center, California Institute of Technology, M/S 314-6, Pasadena, CA 91125, USA
[11] Department of Astronomy, The Oskar Klein Center, Stockholm University, AlbaNova, 10691 Stockholm, Sweden.
[12] Astrophysics Research Centre, School of Mathematics and Physics, Queen's University Belfast, Belfast BT7 1NN, UK
[13] Department of Astronomy, University of California, Berkeley, CA 94720-3411, USA.
[14] Lawrence Berkeley National Laboratory, 1 Cyclotron Road, MS 50B-4206, Berkeley, CA 94720, USA
[15] Department of Physics and Astronomy, University of Southampton, Southampton, SO17 1SX, UK.

with expected luminosity and peak time of $\approx 10^{29} \, \mathrm{erg \, cm^{-2} \, s^{-1} \, Hz^{-1}}$ and $\approx 10 - 30 \, \mathrm{d}$ since explosion, respectively, for relativistic events like SN 1998bw (Galama et al. 1998; Kulkarni et al. 1998; Berger et al. 2003a);

(ii): the GRB jet which, if off-axis, would be observed only when the SN ejecta decelerate to mildly or sub-relativistic speeds, thus producing a delayed and nearly-isotropized radio emission.

Radio is indeed the best wavelength range for identifying relativistic events such as SN 1998bw, and/or off-axis GRBs (Granot & Loeb 2003; Paczynski 2001). In the past, hundreds of SNe Ib/c have been targeted with the Karl G. Jansky Very Large Array (VLA; Berger et al. 2003a; Soderberg et al. 2006c; Bietenholz et al. 2014) and the fraction of SNe Ib/c associated with GRBs has been constrained to $\lesssim 1 - 3\%$. However, only a very small fraction of the Ic SNe targeted by these past studies were broad-lined, the only type of SNe observationally linked to GRBs. Moreover, many of these SNe Ib/c were located in large, massive, and metal-rich hosts, while GRBs are rarely seen in such galaxies (e.g., Modjaz et al. 2008; Levesque et al. 2010; Hjorth et al. 2012; Graham & Fruchter 2013; Perley et al. 2013; Xu et al. 2013; Kelly et al. 2014; Krühler et al. 2015; Perley et al. 2015). Thus, the fraction of purely BL-Ic SNe harboring relativistic jets remained, observationally, largely unconstrained.

Here, we present a sample of 15 SNe discovered by the Palomar Transient Factory and/or intermediate Palomar Transient Factory (PTF/iPTF, hereafter we use PTF for simplicity; Law et al. 2009; Rau et al. 2009), optimized to search for off-axis GRBs, namely, a sample of BL-Ics selected blindly in random galaxies (mostly dwarfs). While all (long-soft) GRBs may be accompanied by BL-Ic SNe, not all of these SNe make GRBs (e.g., Ofek et al. 2007; Soderberg et al. 2010; Milisavljevic et al. 2015). Why should some stars follow a different path to death, ending their lives as collapsars rather than as "ordinary" SNe, is still a mystery. This study aims at providing additional clues to help gain deeper insight into the nature of collapsar events.

After collecting photometric data (Section 2.1) and classifying the SNe in our sample as belonging to the family of BL-Ic SNe (Section 2.2), we performed X-ray follow-up observations for some of the events (Section 2.3) in search for X-ray signatures (not accompanied by γ-rays) from GRBs observed slightly off-axis (and/or "dirty" fireballs; Section 3). We performed cm-wavelength follow-up observations of all the SNe in our sample with the VLA (Section 2.4), in search for SN 1998bw-like radio emission (point (i) above) and/or later-time signatures of off-axis jets (point (ii) above). Our sample greatly enlarges the sample of radio-monitored BL-Ic SNe published over the last ≈ 10 years (Berger et al. 2003a; Soderberg et al. 2006c; Ghirlanda et al. 2013; Bietenholz et al. 2014), and our observational strategy allows us to probe a portion of the radio luminosity-time since explosion phase space that was left largely unexplored by previous studies (Section 4). We constrain the portion of the explosion energy-wind/ISM density parameter space that is excluded under the hypothesis that GRB jets significantly off-axis ($\theta_j \approx 90 \deg$)

are associated with the SNe in our sample (Section 5), and set an upper-limit on the fraction of BL-Ic SNe in our sample that show radio emission possibly compatible with off-axis GRBs expanding in media with densities in the range probed by this study (Section 6). Finally, we give our conclusions (Section 7).

Hereafter, we adopt cosmological parameter values of $H_0 = 69.6 \, \mathrm{km \, s^{-1} \, Mpc^{-1}}$, $\Omega_M = 0.286$, $\Omega_\Lambda = 0.714$ (Wright 2006; Bennett et al. 2014).

2. THE BL-IC SUPERNOVA SAMPLE

2.1. *P48 discovery and photometry*

R-band (or g-band) discoveries (and follow-up) of the SNe in our sample (Table 1) were obtained using the 48-inch Samuel Oschin telescope at the Palomar Observatory (P48), which is routinely used by the PTF/iPTF. Processed images were downloaded from the Infrared Processing and Analysis Center (IPAC) PTF archive (Laher et al. 2014). Photometry was performed relative to the SDSS r-band (or g-band) magnitudes of stars in the field (York et al. 2000). We used our custom pipeline which performs image subtraction, and then point spread function (PSF) photometry on stacks of PTF images extracted from the IPAC archive (Maguire et al. 2012; Ofek et al. 2012, 2013). The flux residuals from individual subtracted images were binned, and converted to magnitudes. Errors were estimated from the standard deviation of the photometric measurements in each bin.

The R-band (or g-band) light curves of the SNe in our sample are shown in Fig. 1. PTF10bzf, PTF10qts, and PTF11qcj photometry was discussed previously in Corsi et al. (2011), Walker et al. (2014), and Corsi et al. (2014) respectively, so we do not present their photometry here (we refer the reader to these papers). The P48 discovery time (T_{P48}), and the maximum R-band (or g-band) absolute magnitudes ($M_{R/g}$) as measured by our P48 monitoring and corrected for Galactic extinction (Schlafly & Finkbeiner 2011), are reported in Table 1. Note that our $M_{R/g}$ is different from the SN light curve peak for cases in which the peak emission was not observed by P48. We do not take into account k-corrections when measuring $M_{r/g}$, but refer the reader to Prentice et al. (2016) and Taddia et al. 2015 (in prep.) for a discussion of these corrections.

2.2. *Spectral classification*

After the discovery with P48, we triggered a spectroscopic follow-up campaign[16] of all the SNe in our sample. PTF10bzf, PTF10qts, and PTF11qcj spectral properties were previously discussed in Corsi et al. (2011), Walker et al. (2014), and Corsi et al. (2014) respectively, so we do not present their spectral analysis here, but we refer the reader to these papers. For the rest of the SNe in our sample, details of the observations are reported in what follows. In Table 1, we also report the estimated redshifts, and the velocities corresponding to the P-Cygni

---

[16] All spectra reported in this work will be made public via WISeREP (Yaron & Gal-Yam 2012).

PTF name -	RA Dec (J2000) (hh:mm:ss deg:mm:ss)	T_{P48}[a] - (MJD)	z - -	d_L - (Mpc)	$M_{R/g}$[b] [AB] (mag)	v (Si) - (km s^{-1})	Ref. - -
10bzf	11:44:02.99 +55:41:27.6	55250.504	0.0498	223	-18.3	2.6×10^4	Corsi et al. (2011)
10qts	16:41:37.60 +28:58:21.1	55413.260	0.0907	418	-19.4	1.7×10^4	Walker et al. (2014)
10xem	01:47:06.88 +13:56:28.8	55470.340	0.0567	255	-18.6	2.0×10^4	This paper
10aavz	11:20:13.36 +03:44:45.2	55514.485	0.062	280	-19.2	1.5×10^4	This paper
11cmh	13:10:21.74 +37:52:59.6	55673.336	0.1055	491	-18.6	1.6×10^4	This paper
11img	17:34:36.30 +60:48:50.6	55755.408	0.158	761	-19.6	1.5×10^4	This paper
11lbm	23:48:03.20 +26:44:33.5	55793.259	0.039	173	-18.0	1.5×10^4	This paper
11qcj	13:13:41.51 +47:17:57.0	55866.520[c]	0.0287	124	-18.0	1.2×10^4	Corsi et al. (2014)
12as	10:01:34.05 +00:26:58.4	55925.298	0.033	146	-17.5	2.2×10^4	This paper
13u	15:58:51.21 +18:13:53.1	56324.481	0.10	463	-18.9	1.0×10^4	This paper
13alq[d]	11:48:02.09 +54:34:38.2	56394.359	0.054	242	-18.9	2.3×10^4	Drake et al. (2013)
13ebw	08:17:15.88 +56:34:41.6	56621.389	0.069	313	-18.2	2.3×10^4	This paper
14dby	15:17:06.29 +25:21:11.4	56832.238	0.074	337	-17.9	1.4×10^4	This paper
14gaq	21:32:54.08 +17:44:35.6	56924.213	0.0826	378	-18.0	1.9×10^4	This paper
15dld[e]	00:58:13.28 -03:39:50.3	57318.322	0.047	210	-17.9	1.0×10^4	This paper/LaSilla-QUEST

[a] Discoveries times (T_{P48}) are from P48 observations in R-band, except for the case of PTF14gaq which was discovered
and observed with P48 in g-band.
[b] $M_{R/g}$ is the maximum absolute magnitude in the P48 R-band for all of the SNe but PTF14gaq, for which $M_{R/g}$ is
measured in the P48 g-band. These magnitudes are corrected for galactic extinction (Schlafly & Finkbeiner 2011).
[c] The SN was visible in a previous g-band image taken on 2011 October 23.
[d] a.k.a. CSS130415:114802+543439/SN 2013bn: PTF13alq was also discovered by the CRTS (Drake et al. 2009) and
classified as a 1998bw-like type Ic SN by the Copernico Telescope in Asiago (Tomasella et al. 2013).
[e] PTF15dld/LSQ15bfp was also discovered by the La Silla-QUEST variability survey (Hadjiyska et al. 2012) and classified
by the Public ESO Spectroscopic Survey of Transient Objects (PESSTO; Smartt et al. 2015).

absorption minimum of the Si II 6355 Å lines, that trace
reasonably closely the position of the photosphere (Maz-
zali et al. 2000, see also Taddia et al. 2015, in prep.).

2.2.1. PTF10xem

On 2010 October 10 UT (≈ 9 d since optical discovery),
we observed PTF10xem with the dual-arm Kast spectro-
graph (Miller & Stone 1993) on the 3 m Shane telescope
at Lick Observatory. We used a 2″wide slit, a 600/4310
grism on the blue side, and a 300/7500 grating on the red
side. Exposure time and air mass were 3600 s and 1.09,
respectively. The derived spectrum shows a good match
with the Ic/BL-Ic SN 2004aw (e.g., Taubenberger et al.
2006) at an epoch of about 15 d since explosion, and with
the BL-Ic SN 2002ap at 6 d since explosion (Fig. 2), so
we classify PTF10xem as a BL-Ic SN.

2.2.2. PTF10aavz

On 2010 November 30 UT (≈ 16 d since optical discov-
ery) we observed PTF10aavz using ISIS on the William
Herschel Telescope (WHT), with a 1.99″wide slit, the
R300B grating set at a central wavelength of ≈ 4500 Å
on the blue side, and the R158R grating set at a cen-
tral wavelength of ≈ 7500 Å on the red side. The expo-
sure time was 1800 s, and mean air mass was 1.17. This
spectrum of PTF10aavz is most similar to the of the
BL-Ic/hyper-energetic and asymmetric SN 2003jd (e.g.,
Valenti et al. 2008; Mazzali et al. 2005) at an epoch of
about 24 d since explosion (Fig. 2).

2.2.3. PTF11cmh

We observed PTF11cmh using ISIS on the WHT on
2011 May 2 UT (≈ 10 d since optical discovery), with a

1.02″wide slit, the R300B grating set at a central wave-
length of ≈ 4500 Å on the blue side, and the R158R
grating set at a central wavelength of ≈ 7500 Å on the
red side. For both the blue and red side observations,
the exposure time was 900 s and the mean air mass was
1.01. The derived spectrum shows a good match with
the Ic/BL-Ic SN 2004aw (e.g., Taubenberger et al. 2006)
at an epoch of about 15 d since explosion, and with the
BL-Ic SN 2002ap at 6 d since explosion (Fig. 2), so we
classify PTF11cmh as a BL-Ic SN.

2.2.4. PTF11img

We observed PTF11img on 2011 August 2 UT (≈ 20 d
since optical discovery), using the Low Resolution Imag-
ing Spectrometer (LRIS; Oke et al. 1995) mounted on
the Keck-I 10 m telescope. The spectrum was taken us-
ing a 1″wide slit, with the 400/8500 grating set at a
central wavelength of ≈ 7800 Å on the red side, and the
600/4000 grism on the blue side. For both sides, the
exposure time and airmass were 600 s and 1.46, respec-
tively. The derived spectrum shows a good match with
both the BL-Ic SN 2002ap (e.g., Gal-Yam et al. 2002;
Mazzali et al. 2002) at 13 d since explosion, and the type
Ic hypernova SN 1997ef (e.g., Iwamoto et al. 1998) at 35 d
since explosion (Fig. 2). We thus classify PTF11img as
a BL-Ic SN.

2.2.5. PTF11lbm

We observed PTF11lbm using ISIS on the WHT on
2011 August 31 UT (≈ 11 d since optical discovery), with
a 1.02″wide slit, the R300B grating set at a central wave-
length of ≈ 4500Å on the blue side; the R158R grating
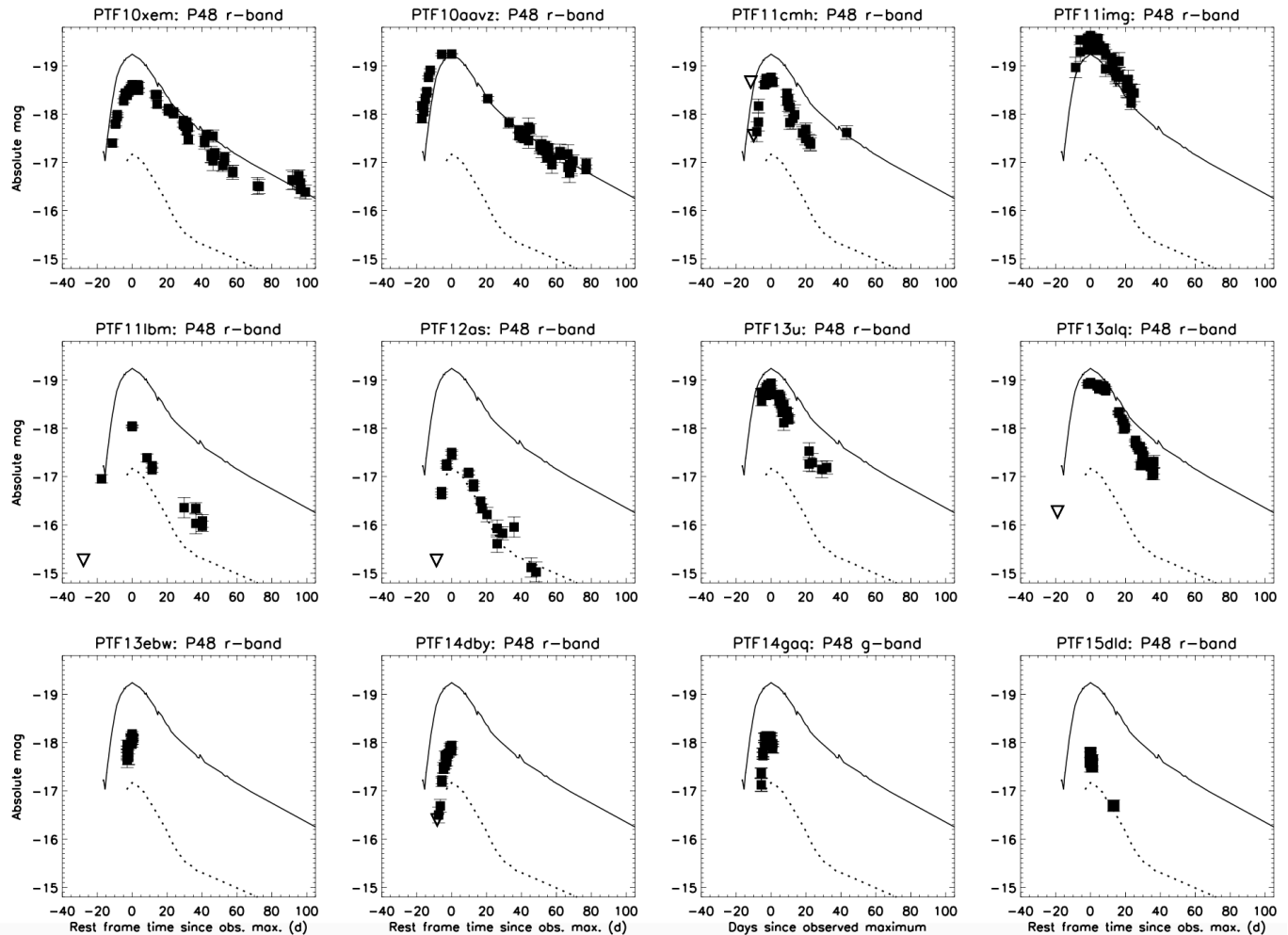set at a central wavelength of ≈ 7500 Å on the red side.

FIG. 1.— The P48 *R*- or *g*-band light curves (corrected for Galactic extinction) of the BL-Ic SNe in our sample. PTF names are reported in the title of each panel. For comparison, we also show the *r*-band light curve of the GRB-associated BL-Ic SN 1998bw (solid line; Clocchiatti et al. 2011), and of the "ordinary" BL-Ic SN 2002ap (dotted line; Pandey et al. 2003). Epochs on the x-axis are measured since the time of maximum emission as observed by P48 (and corrected for redshift effects). Note that the time of maximum as observed by P48 is different from the SN light curve peak time for cases in which the peak emission was not observed by P48.

For both the blue and red side observations, the exposure time was 900 s. The mean air mass was about 1.01. The derived spectrum shows a good match with both the BL-Ic SN 2002ap (e.g., Gal-Yam et al. 2002; Mazzali et al. 2002) at 6 d since explosion, and the type Ic hypernova SN 1997ef (e.g., Iwamoto et al. 1998) at 35 d since explosion (Fig. 2). We thus classify PTF11lbm as a BL-Ic SN.

2.2.6. *PTF12as*

We observed PTF12as on 2012 January 2 UT (≈ 2 d since optical discovery), using the Dual Imaging spectrograph (DIS) mounted on the 3.5 m telescope at the Apache Point Observatory. The spectrum was taken using a 1.5″wide slit, with a B400/R300 grating setup. The exposure time and airmass were 1000 s and 1.50, respectively. The derived spectrum shows a good match with the GRB-associated BL-Ic SN 2002ap (e.g., Mazzali et al. 2002; Gal-Yam et al. 2002) at 6 d since explosion (Fig.

2).

2.2.7. *PTF13u*

On 2013 February 18 UT (≈ 17 d since optical discovery) we observed PTF13u with the Double Beam Spectrograph (DBSP; Oke & Gunn 1982) on the Palomar 200-inch telescope (P200). We used the 316/7500 and 600/4000 gratings for red and blue camera respectively, with a D55 dichroic, resulting in a spectral coverage of $\approx (3500 - 9500)$ Å. Exposure times and air mass were of 590 s and 1.06, respectively. This spectrum of PTF13u matches that of the BL-Ic/hyper-energetic and asymmetric SN 2003jd (e.g., Valenti et al. 2008; Mazzali et al. 2005) at ≈ 29 d since explosion (Fig. 2).

2.2.8. *PTF13alq*

On 2013 April 13 UT (≈ 1 d since optical discovery) we observed PTF13alq with the DBSP (Oke & Gunn 1982) on P200. We used the 316/7500 and 600/4000
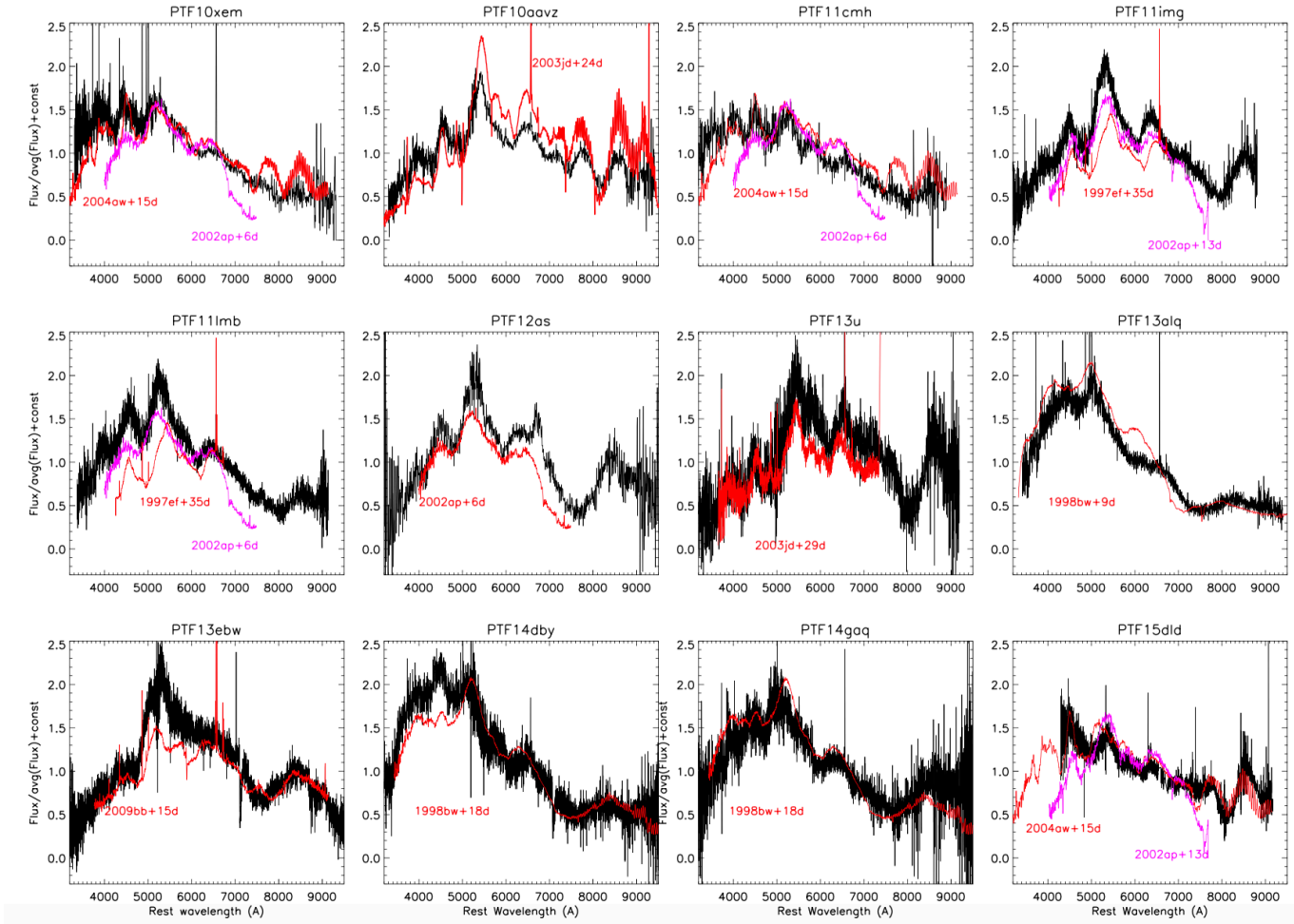
Fɪɢ. 2.— Spectra of the SNe BL-Ic in our sample (black) compared to the spectra of the of the hypernova SN 1997ef (Iwamoto et al. 1998; Branch 1999, epoch calculated since 1997 November 15), of the GRB-associated BL-Ic SN 1998bw (epoch calculated since 1998 April 25; Patat et al. 2001), of the BL-Ic SN 2002ap (epoch calculated since 2002 January 28; Gal-Yam et al. 2002; Mazzali et al. 2002), of the BL-Ic/hyper-energetic and asymmetric SN 2003jd (epoch calculated since 2003 October 21; Valenti et al. 2008; Mazzali et al. 2005; Soderberg et al. 2006c), of the Ic/BL-Ic SN 2004aw (epoch calculated assuming an explosion date of ≈ 15 d before maximum; Taubenberger et al. 2006), and of the relativistic BL-Ic SN 2009bb (epoch calculated since 2009 March 19; Soderberg et al. 2010; Pignata et al. 2011). (See the electronic version of this paper for colors.)

gratings for red and blue camera respectively, with a D55 dichroic, resulting in a spectral coverage of $\approx (3500 - 9500)$ Å. Exposure times and air mass were of 300 s and 1.1, respectively. The derived spectrum shows a good match with the GRB-associated BL-Ic SN 1998bw (e.g., Patat et al. 2001) at 9 d since explosion (Fig. 2).

2.2.9. *PTF13ebw*

We observed PTF13ebw on 2013 December 4 UT ($\approx$ 9 d since optical discovery), using LRIS mounted on the Keck-I 10 m telescope. The spectrum was taken using a 1″wide slit, with the 400/8500 grating set at a central wavelength of ≈ 7800 Å on the red side, and the 600/4000 grism on the blue side. The exposure time and airmass were 500 s and 1.36, respectively. The derived spectrum shows a good match with the relativistic BL-Ic SN 2009bb (Soderberg et al. 2010) at 15 d since explosion (Fig. 2).

2.2.10. *PTF14dby*

On 2014 June 29 (≈ 5 d since optical discovery), we observed PTF14dby with LRIS mounted on the Keck-I 10 m telescope. The spectrum was taken using a 1″wide slit, with the 400/8500 grating set at a central wavelength of ≈ 7800 Å on the red side, and the 400/3400 grism on the blue side. The exposure time and airmass were 300 s and 1.19, respectively. This spectrum of PTF14dby reveals a good match with the GRB-associated BL-Ic SN 1998bw (e.g., Patat et al. 2001) at ≈ 18 d since explosion (Fig. 2).

2.2.11. *PTF14gaq*

We observed PTF14gaq on 2014 October 1 UT (≈ 7 d since optical discovery) with the DBSP on P200. We used the 316/7500 and 600/4000 gratings for the red and blue camera respectively, with a D55 dichroic, resulting in a spectral coverage of $\approx (3500 - 9500)$ Å. Exposure times and air mass were of 600 s and 1.05, respectively.

This spectrum of PTF14gaq shows a good match with the GRB-associated SN 1998bw (e.g., Patat et al. 2001) at $\approx$ 18 d since explosion (Fig. 2).

2.2.12. *PTF15dld*

We observed PTF15dld on 2015 November 7 UT ($\approx$ 15 d since the P48 optical discovery) with the Deep Extragalactic Imaging Multi-Object Spectrograph (DEIMOS) mounted on the Keck-II 10 m telescope. The spectrum was taken using the 600ZD grating and GG455 filter. The exposure time and airmass were 600 s and 1.11, respectively. The derived spectrum shows a good match with both the BL-Ic SN 2002ap (e.g., Gal-Yam et al. 2002; Mazzali et al. 2002) at 13 d since explosion, and with the Ic/BL-Ic SN 2004aw (e.g., Taubenberger et al. 2006) at an epoch of about 15 d since explosion (Fig. 2).

2.3. *Swift/XRT follow-up and data reduction*

None of the BL-Ic SNe in our sample was found to be spatially coincident with any of the well-localized GRB in the *Swift* (Gehrels et al. 2004) catalog. For some of the events, we triggered *Swift*/XRT (Burrows et al. 2005) follow-up observations via our approved Target of Opportunity Programs[17] in order to further exclude the presence of a GRB X-ray afterglow with no associated γ-rays (as would be the case for a GRB jet observed slightly off-axis, or for a so-called "dirty" fireball; see e.g. Rhoads 2003).

We downloaded the *Swift*-XRT data from the archive[18]. None of the SNe in our sample yielded a detection with *Swift*/XRT, so we calculated 3σ upper-limits on the 0.3-10.0 keV count rate using standard analysis procedures. The upper-limits are reported in Table 2, where we have converted the 0.3-10 keV XRT count rates into fluxes assuming a photon index of $\Gamma_X = 2$ and correcting for Galactic absorption.

X-ray observations of PTF11qcj obtained with *Swift*/XRT and *Chandra*/ACIS (Garmire et al. 2003) were previously presented in Corsi et al. (2014). We include some of these observations (the most significant *Chandra*/ACIS detection and the deepest *Swift*/XRT upper-limit) in Table 2 for completeness.

2.4. *VLA follow-up observations and data reduction*

We observed all of the SNe in our sample, along with the necessary calibrators, with the VLA[19] (Perley et al. 2009) under our Target of Opportunity programs[20]. VLA data were reduced and imaged using the Common Astronomy Software Applications (CASA) package.

The VLA flux measurements and/or upper-limits are reported in Table 3. Measurement errors are calculated

---

[17] Program IDs 1013248 and 1114155 (PI: Corsi).
[18] See http://heasarc.gsfc.nasa.gov/cgi-bin/W3Browse/swift.pl.
[19] The National Radio Astronomy Observatory is a facility of the National Science Foundation operated under cooperative agreement by Associated Universities, Inc.; http://www.nrao.edu/index.php/about/facilities/vlaevla
[20] VLA/11A-227, VLA/11B-034, VLA/12B-247, VLA/14A-434, and VLA/15A-314 - PI: A. Corsi; and VLA/10B-221 - PI: Kasliwal).
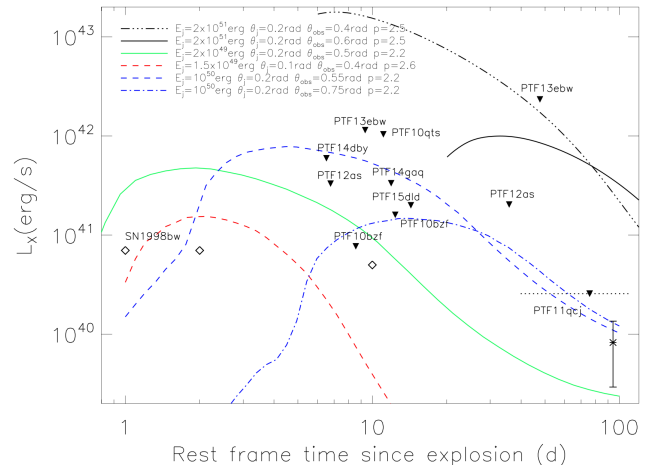

FIG. 3.— *Swift*/XRT upper-limits on some of the BL-Ic SNe in our sample (downward pointing triangles) compared with the X-ray emission from GRB 980425 (diamonds) and with the X-ray emission expected from off-axis GRB models by van Eerten & MacFadyen (2011); van Eerten et al. (2012). GRB jets opening angles are set to $\theta_j = (0.1 - 0.2)$ rad; the medium is a constant density ISM ($n_{ISM} = 1 - 10 \, cm^{-3}$); observer's viewing angles are in the range $\theta_{obs} \approx (2-4)\theta_j$. The fraction of energy density of the ejecta going into electrons (ϵ_e) and magnetic fields (ϵ_B) are both set to 0.1 in all of the above models. For PTF11qcj we plot the flux obtained from the most significant *Chandra*/ACIS detection after subtracting the possible host galaxy contribution (asterisk), and the deepest *Swift*/XRT upper limit (dotted line). We attribute the X-ray emission from PTF11qcj to the presence of strong CSM interaction rather than to a GRB X-ray afterglow. See Corsi et al. (2014) for a complete discussion. (See the electronic version of this paper for colors.)

by adding in quadrature the rms map error, and a basic fractional error ($\approx 5\%$) which accounts for inaccuracies of the flux density calibration (Weiler et al. 1986; Ofek et al. 2011).

3. X-RAY CONSTRAINTS ON ASSOCIATED GRB X-RAY AFTERGLOWS

As mentioned in the previous Section, none of the SNe in our sample are spatially coincident with any well-localized GRB. For a limited number of these SNe, our observations with the *Swift*/XRT allow us to make some comparisons with the X-ray light curve that would be expected from an accompanying GRB 980425-like event, or from a high-luminosity GRB observed slightly off-axis. For the last, we use the numerical model by van Eerten & MacFadyen (2011); van Eerten et al. (2012), which considers a relativistic GRB fireball expanding in a uniform density medium.

As evident from Fig. 3, while *Swift*/XRT upper-limits can exclude X-ray afterglows associated with high-luminosity (high-energy) GRBs observed slightly off-axis (up to $\theta_{obs} \lesssim (2-3)\theta_j$), X-ray emission as faint as the afterglow of the low-luminosity GRB 980425 cannot be excluded. As we discuss in Section 4, radio data collected with the VLA enable us to exclude 1998bw-like emission for most of the SNe in our sample.

For PTF11qcj, *Chandra* observations yielded a detection but we attribute this X-ray emission to the presence of strong CSM interaction rather than to a GRB X-ray

TABLE 2
3σ X-ray upper-limits or detections for some of the SNe in our sample.

PTF name	Date (MJD)	ΔT_X[f] (days)	Instrument -	Band (keV)	Exp. (ks)	N_H[g] $(10^{20}\,\mathrm{cm}^{-2})$	Count Rate $(10^{-4}\,\mathrm{s}^{-1})$	Flux (unabs)[h] $(10^{-14}\,\mathrm{erg\,cm}^{-2}\,\mathrm{s}^{-1})$	Ref.
10bzf	55259.290	9	*Swift*-XRT	0.3-10	5.0	0.88	< 3.7	< 1.3	Kasliwal & Cenko (2010)
”	55263.303	13	*Swift*-XRT	0.3-10	5.0	”	< 7.7	< 2.7	Kasliwal & Cenko (2010)
10qts	55426.126	13	*Swift*-XRT	0.3-10	4.9	2.7	< 4.2	< 1.6	This paper
11qcj	55920.045	78	*Swift*-XRT	0.3-10	31.4	1.0	< 4.1	< 1.4	Corsi et al. (2014)
”	55939.05	97	*Chandra*-ACIS	0.3-8.0	9.8	”	8.8 ± 3.3[i]	0.76 ± 0.26	Corsi et al. (2014)
12as	55932.340	7	*Swift*-XRT	0.3-10	4.6	2.5	< 33	< 13	This paper
”	55962.150	37	*Swift*-XRT	0.3-10	4.9	”	< 21	< 8.0	This paper
13ebw	56631.719	10	*Swift*-XRT	0.3-10	4.8	4.6	< 24	< 9.8	This paper
”	56672.486	51	*Swift*-XRT	0.3-10	2.4	”	< 48	< 20	This paper
14dby	56839.043	7	*Swift*-XRT	0.3-10	9.5	4.2	< 11	< 4.4	This paper
14gaq	56936.081	12	*Swift*-XRT	0.3-10	7.8	6.9	< 14	< 6.1	This paper
15dld	57332.973	15	*Swift*-XRT	0.3-10	9.9	3.2	< 9.8	< 3.8	This paper

[f] Epoch in days since P48 discovery (see Table 1), not corrected for redshift effects.
[g] Hydrogen column densities are weighted averages from the Leiden/Argentine/Bonn (LAB) Survey of Galactic H I (Kalberla et al. 2005).
[h] The count-rate-to-flux conversion assumes a photon index of $\Gamma_X = 2$.
[i] *Chandra* observations of PTF11qcj yielded detections which we attribute to the presence of strong CSM interaction rather than to a GRB X-ray afterglow. Some host galaxy contamination to the measured X-ray flux might also be present. See Corsi et al. (2014) for a complete discussion.

afterglow. See Corsi et al. (2014) for a complete discussion.

4. CONSTRAINING THE FRACTION OF 1998BW-LIKE EVENTS USING RADIO EMISSION

Here, we aim at observationally constraining the fraction of BL-Ic SNe with radio luminosities comparable to that of the GRB-associated SN 1998bw (Kulkarni et al. 1998) to ultimately constrain the fraction of BL-Ic SNe harboring low-luminosity GRBs. Indeed, most of the GRBs with an associated and spectroscopically confirmed SN are low-luminosity bursts ($E_{\gamma,iso} \lesssim 10^{50}$ ergs), although notable exceptions are GRB 030329 (Stanek et al. 2003) and GRB 130427A (e.g., Melandri et al. 2014; Perley et al. 2014). The fraction of BL-Ic SNe harboring low-luminosity GRBs was left largely unconstrained by previous efforts (Berger et al. 2003a; Soderberg et al. 2006c; Bietenholz et al. 2014) due to the very small number of BL- Ic events with radio follow-up available to the community.

Theoretical studies have indirectly constrained the fraction of BL-Ic SNe harboring low-luminosity GRBs by constraining the local rate of low-luminosity GRBs (via luminosity function fitting) and then comparing this estimated local rate with the rate of BL-Ic SNe collected via optical surveys. Following this approach, Guetta & Della Valle (2007) derived that $\gtrsim 10\%$ of BL-Ic SNe are accompanied by low-luminosity GRBs. This is consistent with the earlier results by Podsiadlowski et al. (2004), who found that the rates of GRBs and BL-Ic SNe are comparable to within the uncertainties, and their ratio likely $\gtrsim 30\%$ (see Table 1 in Podsiadlowski et al. 2004). More recently, following a statistical approach inspired by the Drake equation, Graham & Schady (2015) estimated that there are 4000 ± 2000 BL-Ic SNe in low-metallicity environments for every (long) GRB aligned in our direction. This number is a composite of the fraction of such SNe which produce GRBs and the fraction that are beamed in our direction, and would imply that $\lesssim 5\%$ of the BL-Ic SNe are associated with a GRB.

With our PTF discoveries, we now have a sample of 15 BL-Ic SNe discovered *independently of a GRB trigger*, with at least one radio follow-up observation on

timescales $\lesssim 300$ d since explosion (as measured in the SN rest frame; Figs. 4 and 5). Of these 15 SNe, 12 have been uniquely observed via our VLA programs. Our observations have greatly enlarged the sample of 8 BL-Ic SNe with radio follow-up at $\lesssim 300$ d collected via independent efforts during the last decade (Fig. 4, yellow; Fig. 5, green, yellow, and magenta asterisks; Berger et al. 2003a; Chomiuk & Soderberg 2010; Soderberg et al. 2010; Soderberg & Chomiuk 2011; Drake et al. 2013; Kamble & Soderberg 2013; Salas et al. 2013; Chakraborti et al. 2015; Milisavljevic et al. 2015). We are thus in a position to start constraining the theoretical expectations for the low-luminosity GRB-to-BL-Ic SN ratio using a direct observational signature: the presence (or absence) of 1998bw-like radio emission.

In Figs. 4 and 5, the 5 GHz radio light curve of SN 1998bw is compared with the upper-limits and detections obtained for the SNe in our sample (4.8-6.3 GHz; See Table 3). As evident from Fig. 5, we have 3 SNe (PTF11cmh, PTF11qcj, and PTF14dby) that show bright radio emission, much brighter than the ordinary BL-Ic SN 2002ap and almost at the level of SN 1998bw, but their radio peak occurs $\gtrsim 5\times$ later than for SN 1998bw. Thus, as we explain in the following Section, we consider these SNe as observationally different from SN 1998bw, likely related to events on the dividing line between ordinary SNe and GRBs, although an interpretation as off-axis GRB jets might also be possible. For the remaining 12 SNe in our sample, we detect no radio emission and set upper-limits (Fig. 4, black downward-pointing triangles). For 10 of these 12 SNe (all but PTF10xem and PTF13u), we have at least one upper-limit which constrains the radio emission to be dimmer than the emission of SN 1998bw *at a similar epoch*, thus excluding a radio light curve observationally similar to that of the prototype relativistic BL-Ic SN 1998bw. (We note that 8 out of the 12 SNe also exclude radio emission similar to SN 2009bb, a relativistic BL-Ic SN with no associated GRB; Soderberg et al. 2010).

Based on the above results, we conclude that of the 10+3 PTF SNe whose radio observations can set constraints on SN 1998bw-like emission, none of them was

in fact like SN 1998bw in the radio i.e., they were all *observationally* different. Adding to this sample the BL-Ic SN 2002ap (Gal-Yam et al. 2002; Mazzali et al. 2002) and SN 2002bl (Armstrong et al. 2002; Berger et al. 2003a), and the CSM-interacting BL-Ic SN 2007bg (Salas et al. 2013), we have a total of 16 BL-Ic SNe for which radio emission observationally similar to SN 1998bw is excluded. Because the 99.865% confidence (3σ Gaussian equivalent for a single-sided distribution) Poisson upper-limit on zero SNe compatible with SN 1998bw is ≈ 6.61, we conclude that the rate of BL-Ic SNe observationally similar to SN 1998bw $\lesssim 6.61/16 \approx 41\%$.

We note that for these 16 SNe we also exclude on-axis radio emission typical of long GRB afterglows at cosmological distances (blue line and shaded area in Fig. 4; see Chandra & Frail 2012), and radio emission observationally similar to that of the low-luminosity GRB 031203. However, none of our upper-limits exclude radio emission similar to GRB 060218. This is not surprising since the afterglow of this low-luminosity GRB faded on timescales much faster than the ones our VLA monitoring campaign was designed to target (peak timescales of $\approx 20 - 30$ d). Finally, only some of our upper-limits exclude radio afterglow emission similar to that of the low-luminosity GRB 100316D (although a more quantitative comparison with this burst is hampered by its poorly sampled radio light curve).

5. CONSTRAINING THE FRACTION OF (LARGELY) OFF-AXIS GRBS FROM RADIO NON-DETECTIONS

Low-luminosity GRBs (such as GRB 980425 associated with SN 1998bw) are believed to be intrinsically less energetic events (when compared to high-luminosity ones) with jet opening angles $\gtrsim 30$ deg (e.g., Liang et al. 2007). However, the possibility that low-luminosity GRBs are higher-energy events observed off-axis has also been discussed (e.g., Waxman 2004b; Ramirez-Ruiz et al. 2005). Indeed, most (high-luminosity) GRBs are believed to have opening angles of the order of ~ 10 deg (e.g., Frail et al. 2001; Liang et al. 2008; Racusin et al. 2009; Zhang et al. 2015). Here, we aim at answering the question of whether the BL-Ic SNe in our sample that do not show evidence for radio emission observationally similar to that of SN 1998bw (Section 4) could still be accompanied by an off-axis ($\theta_{obs} \approx 90$ deg) GRB afterglow that would become visible in the radio band long past the explosion (at timescales of the order of ~ 1 yr; Levinson et al. 2002; Waxman 2004b; Gal-Yam et al. 2006), when the relativistic fireball enters the sub-relativistic phase and starts spreading, rapidly intersecting the viewer's line of sight while approaching spherical symmetry. Our upper-limits add to the late-time ones that have been collected in the past ($t \gtrsim 500$ d since explosion, not plotted in Figs. 4-5; see Soderberg et al. 2006c; Bietenholz et al. 2014).

We model the late-time radio emission from an off-axis GRB following the works by Livio & Waxman (2000) and Waxman (2004b), modified to account for the results of more recent numerical simulations (Zhang & MacFadyen 2009; van Eerten & MacFadyen 2012). The last have shown that at the end of the Blandford-McKee (BM) phase, the fireball becomes non relativistic but, differently from what previously thought, the transition to the spherical Sedov-Neumann-Taylor (SNT) blast wave
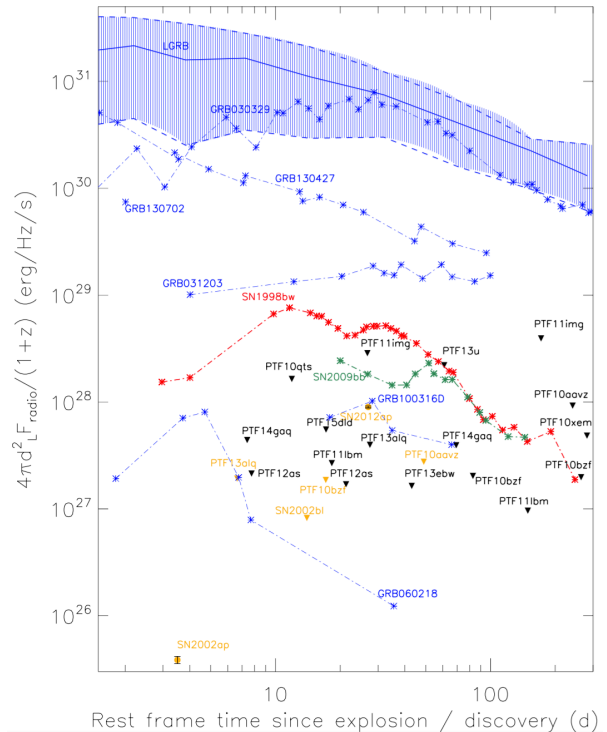

FIG. 4.— Radio (observed central frequencies of $\approx 4.8 - 6.3$ GHz; see Table 3) upper-limits for the BL-Ic SNe in our sample with VLA follow-up observations at $t \lesssim 300$ d since discovery (as measured in the SN rest frame), compared with: the mean radio (8.5 GHz) light curve of cosmological GRBs (blue solid line) as derived by Chandra & Frail (2012), together with the 75% confidence interval (blue shaded region); radio (≈ 5 GHz) afterglow light curves of long GRBs with spectroscopically-associated SNe (blue asterisks; Berger et al. 2003b; Soderberg et al. 2004; Frail et al. 2005; Soderberg et al. 2006b; Margutti et al. 2013; Perley et al. 2014; Singer et al. 2015); the light curve of the GRB-SN 1998bw (red asterisks; Kulkarni et al. 1998); the light curve of the relativistic BL-Ic SN 2009bb (green asterisks; Soderberg et al. 2010) and SN 2012ap (yellow dot; Chakraborti et al. 2015; Milisavljevic et al. 2015). Black triangles are our upper-limits. Yellow data points or upper-limits are for BL-Ic SN radio ($\approx 5 - 8.5$ GHz) follow-up observations that were not conducted via our programs (Berger et al. 2003a; Chomiuk & Soderberg 2010; Soderberg et al. 2010; Soderberg & Chomiuk 2011; Kamble & Soderberg 2013). Radio detections for the PTF sample are plotted in Fig. 5. Late-Time radio observations of BL-Ic SNe performed at $t \gtrsim 300$ d since explosion via other studies (Soderberg et al. 2006c; Bietenholz et al. 2014) are not reported here.

takes a rather long time. Thus, accurate modeling of the fireball evolution over timescales in between the BM and SNT phases (which are relevant for this study) requires numerical simulations. However, Zhang & MacFadyen (2009) have shown that for fireballs expanding in a medium of constant density $n_{0,ISM}$ (in units of cm^{-3}) and at timescales

$$t \gtrsim (1 + z) \times t_{\rm SNT}/2, \qquad (1)$$

where

$$t_{\rm SNT} \approx 92\,{\rm d} \left(\frac{E_{51}}{n_{0,ISM}}\right)^{1/3}, \qquad (2)$$

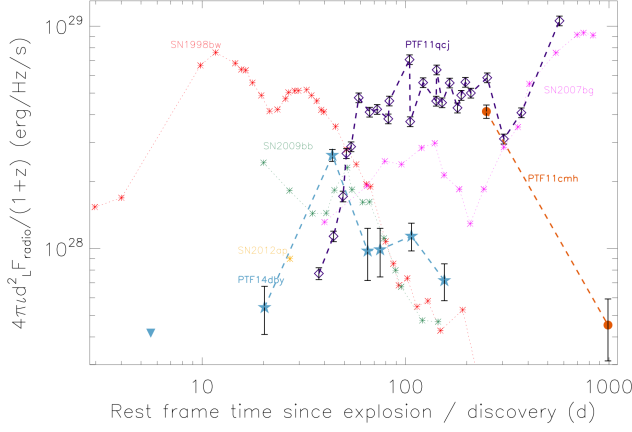an acceptable analytical approximation to the afterglow

Fig. 5.— BL-Ic SNe in our sample with radio detections: PTF11cmh, orange dots; PTF11qcj, purple diamonds (Corsi et al. 2014); PTF14dby, blue stars. We compare these non-relativistic / CSM-interacting SNe with the light curves of the GRB-SN 1998bw (red asterisks; Kulkarni et al. 1998), of the relativistic BL-Ic SN 2009bb (green asterisks; Soderberg et al. 2010), of the CSM-interacting BL-Ic SN 2007bg (magenta asterisks; Salas et al. 2013), and of the relativistic SN 2012ap (yellow asterisk; Chakraborti et al. 2015). As evident from this comparison, the non-relativistic and CSM-interacting BL-Ic peak at later timescale than the relativistic ones.

flux is given by:

$$F_\nu(t) \approx 0.16 \, d_{L,28}^{-2} (1+z)^{\frac{1}{2}} \left(\frac{\epsilon_e}{0.1} \right) \left(\frac{\epsilon_B}{0.1} \right)^{3/4} n_{0,ISM}^{\frac{9}{20}} E_{51}^{\frac{13}{10}}$$
$$\times \left(\frac{\nu}{1 \, \text{GHz}} \right)^{-1/2} \left(\frac{t}{92 \, \text{d}(1+z)} \right)^{-9/10} \text{mJy.} \quad (3)$$

Here E_{51} is the beaming-corrected ejecta energy in units of 10^{51} erg; ϵ_e and ϵ_B are the fraction of ejecta energy density going into electrons and magnetic fields, respectively; $d_{L,28}$ is the luminosity distance of the source in units of 10^{28} cm; z is the source redshift; and the power-law index of the electron energy distribution has been set to $p \approx 2$.

Equation (3) corresponds to Eq. (15) in Waxman (2004b) where, however, the dependence on t_{SNT} has been eliminated by using our Eq. (2) (or, equivalently, Eq. (11) in Waxman 2004b). Using Eq. (3) to constrain the fireball parameters by comparison with observations taken at timescales t that satisfy Eq. (1), yields constraints on the (beaming-corrected) energy that are accurate to within a factor of ≈ 2 (see Fig. 10 in Zhang & MacFadyen 2009).

By imposing

$$t \gtrsim t_{\text{SNT}} \qquad F_\nu(t) \gtrsim F_{obs,\nu}(t), \quad (4)$$

we thus calculate, for the SNe in our sample (Table 3), the values of (beaming corrected) energy and medium density that would give a radio luminosity above our upper-limit $F_{obs,\nu}(t)$, at the time t of our observation. The exclusion regions obtained in this way are shown in Fig. 6. In this Figure we have set the micro-physics parameters equal to their median values as estimated by Santana et al. (2014) i.e., $\epsilon_e \approx 0.22$ and $\epsilon_B \approx 0.01$. However, these parameters (and especially ϵ_B) vary within

large ranges, $0.02 \lesssim \epsilon_e \lesssim 0.6$ and $3 \times 10^{-5} \lesssim \epsilon_B \lesssim 0.33$ (Santana et al. 2014). As evident from Eq. (3), for a given upper-limit on the flux at a certain epoch, the smaller the value of the product $\epsilon_e \epsilon_B^{3/4}$, the larger the minimum E_{51} excluded for each value of n_0 (thus, off-axis emission from lower-energy fireballs / low-luminosity GRBs is less constrained).

In Fig. 7 we use our upper-limits to set similar constraints on off-axis GRBs expanding in a wind medium. In this case, the expected radio flux is approximated as (Waxman 2004b; Soderberg et al. 2006c):

$$F_\nu(t) \approx 0.053 \, d_{L,28}^{-2}(1+z)^{1/2} \left(\frac{\epsilon_e}{0.1} \right) \left(\frac{\epsilon_B}{0.1} \right)^{3/4} A_*^{3/4} E_{51}$$
$$\times \left(\frac{\nu}{1 \, \text{GHz}} \right)^{-1/2} \left(\frac{t}{92 \, \text{d}(1+z)} \right)^{-3/2} \text{mJy}, \quad (5)$$

where A_* is the circumstellar density, which is related to progenitor mass loss-rate $\dot{M}$ and wind velocity v_w as $A_* = (\dot{M}/10^{-5} M_\odot \text{yr}^{-1})/(v_w/1000 \, \text{km s}^{-1})$; and where we have used (Waxman 2004b; Soderberg et al. 2006c):

$$t_{\text{SNT}} \approx 92 \, \text{d} \left(\frac{E_{51}}{A_*} \right). \quad (6)$$

We note that Eq. (5) corresponds to Eq. (14) in Waxman (2004b) where the dependence on t_{SNT} is eliminated by using our Eq. 6 (or, equivalently, Eq. (8) in Waxman 2004b). Here we are assuming that the conclusions reached by Zhang & MacFadyen (2009) for the constant density case are valid also for a fireball expanding in a wind medium, namely, that Eq. (5) provides an estimate of the fireball parameters good to within a factor of ≈ 2 when compared to flux measurements carried out at epochs $t \gtrsim t_{\text{SNT}}$.

We can compare the results shown in Figs. 6-7 with the energy and density derived from the broad-band afterglow modeling of the high-luminosity GRB 030329 (for which $\theta_j \approx 5 - 17 \deg$, $E_{51} = 0.67$, $n_{0,ISM} \approx 3$; Berger et al. 2003c; Soderberg et al. 2006c) and GRB 130427A (for which $E_{51} \gtrsim 0.5$, $\theta_j \gtrsim 5 \deg$, and $0.01 \lesssim A_* \lesssim 0.05$; Perley et al. 2014), and of the low-luminosity GRB 980425 (for which $E_{51} \approx 0.05$ and $A_* \approx 0.04$; Waxman 2004a,b; Soderberg et al. 2006c) and GRB 031203 (for which $E_{51} = 0.017$ and $n_{0,ISM} = 0.6$; Soderberg et al. 2004; Ramirez-Ruiz et al. 2005; Soderberg et al. 2006c). From such a comparison we conclude that most of the SNe in our sample exclude GRBs with (beaming corrected) energy and ISM density comparable to GRB 030329, observed largely off-axis and/or during the non-relativistic phase. On the other hand, our upper-limits cannot exclude a GRB as sub-energetic as GRB 980425 observed during its non-relativistic phase, nor an off-axis GRB expanding in a low-density environment such as GRB 031203 and GRB 130427A.

As discussed before, our conclusions depend somewhat on the assumed values of the micro-physics parameters. Indeed, as evident from Eq. (5), also in a wind environment the smaller the value of the product $\epsilon_e \epsilon_B^{3/4}$, the larger the minimum E_{51} excluded for each value of A_*.

6. VLA DETECTIONS: PTF11CMH AND PTF14DBY

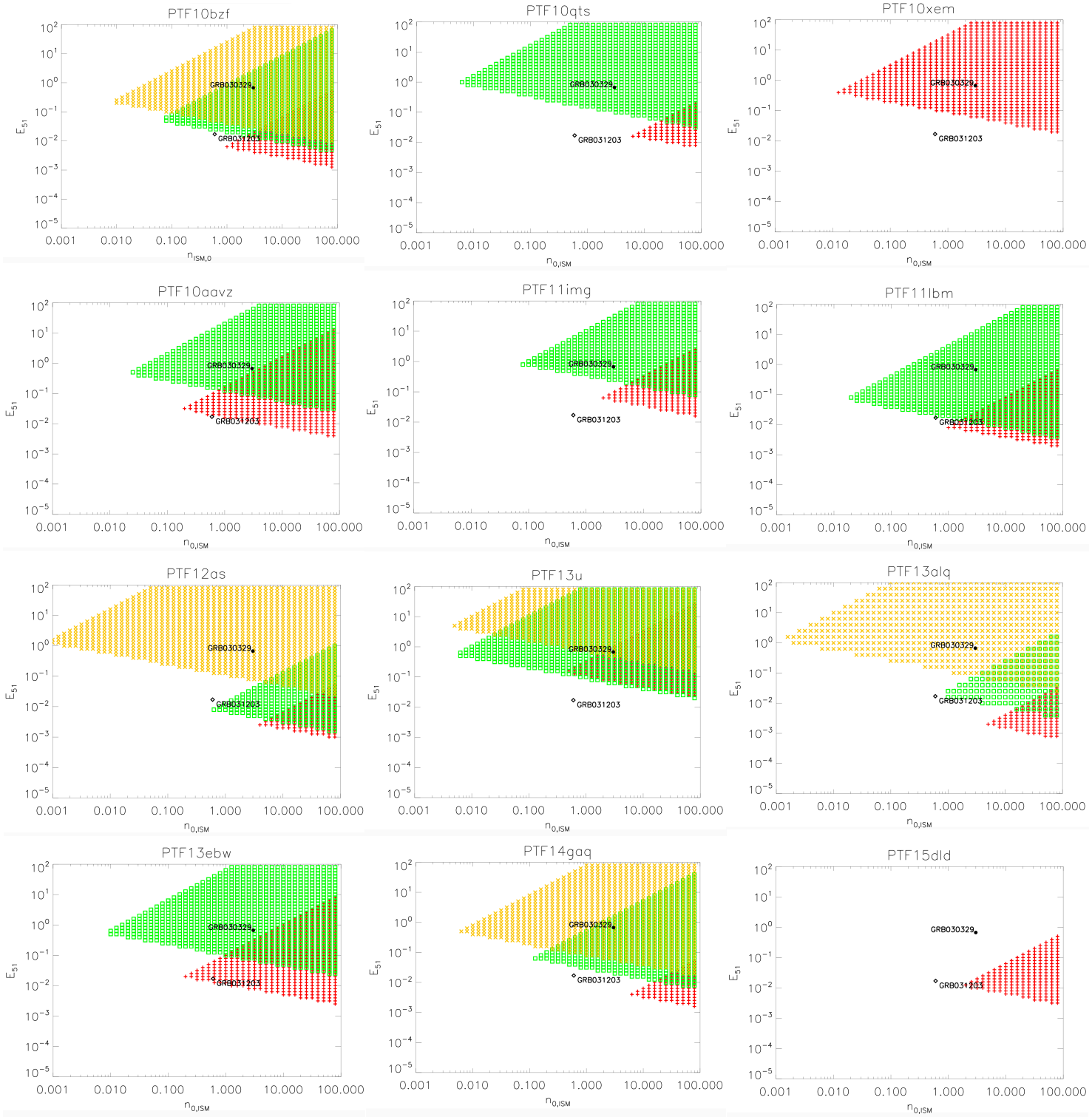Non-thermal (self-absorbed) synchrotron radiation can be emitted from SN or GRB ejecta during interaction

FIG. 6.— Regions of the energy (E_{51}) - density ($n_{0,ISM}$) parameter space excluded by our VLA upper-limits. For each SN in our sample, red, green, and yellow colors correspond to different observations. Specifically, for each SN, we use red for the constraints derived from the first epoch of observations, green for the second epoch (if observed twice; see Table 3), and yellow for the third epoch (if available; see Table 3).
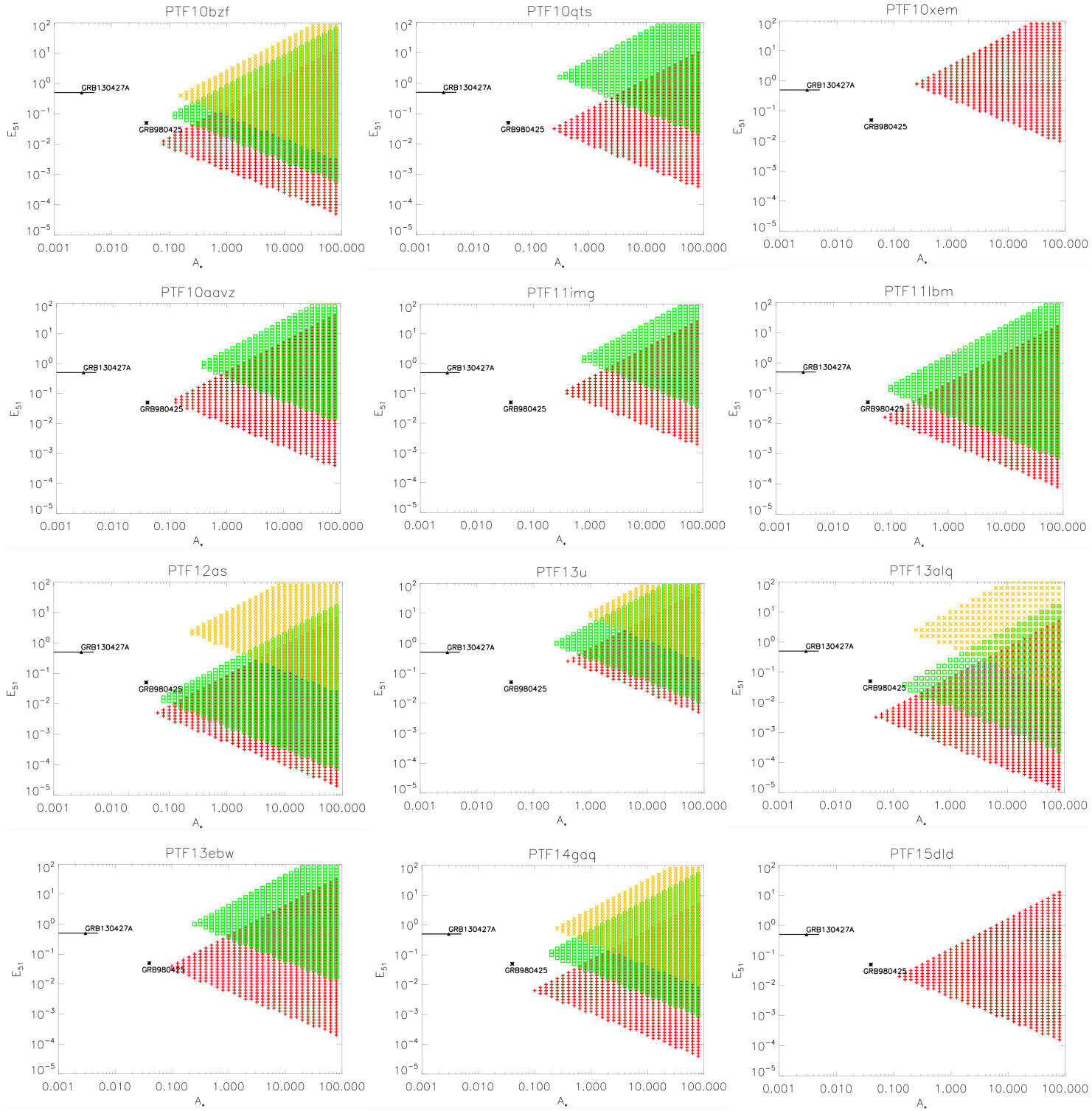
FIG. 7.— Regions of the energy (E_{51}) - density (A_*) parameter space excluded by our VLA upper-limits. For each SN in our sample, red, green, and yellow colors correspond to different observations. Specifically, for each SN, we use red for the constraints derived from the first epoch of observations, green for the second epoch (if observed twice; see Table 3), and yellow for the third epoch (if available; see Table 3).
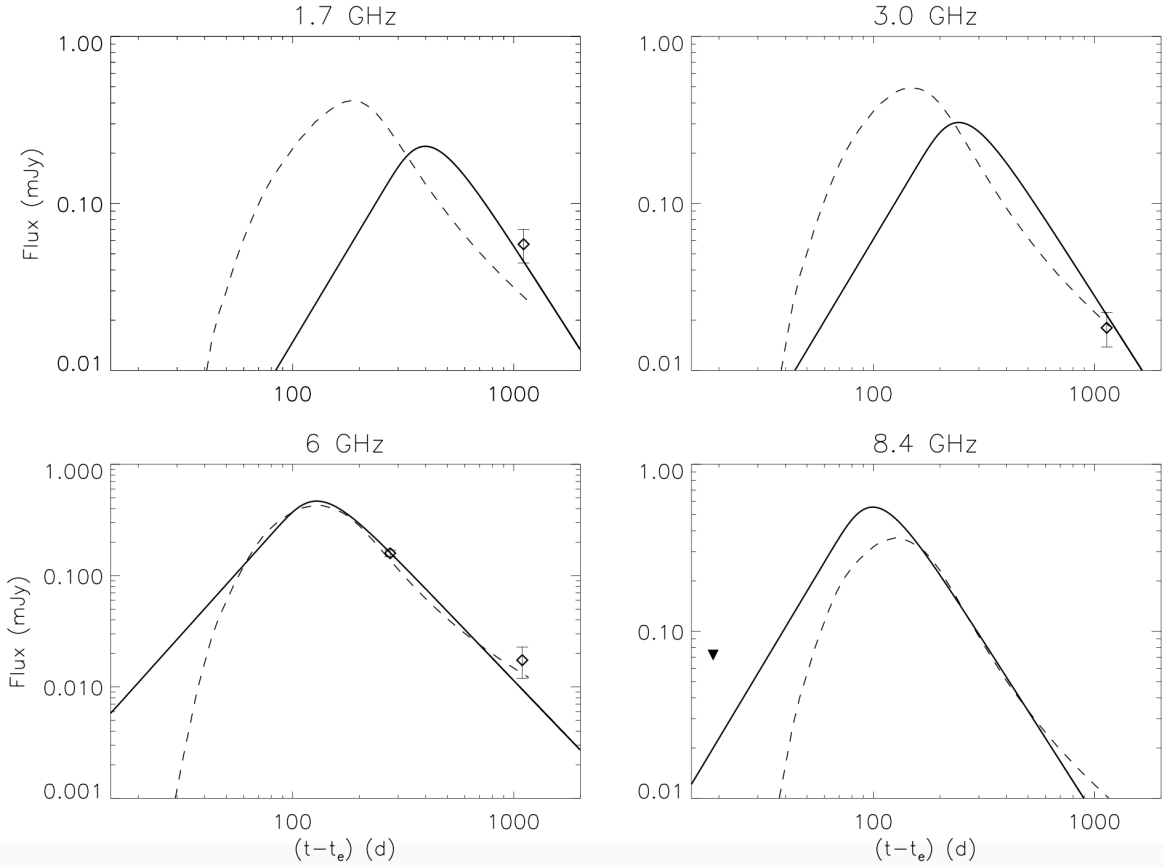
FIG. 8.— Best fit radio light curves of PTF11cmh in the synchrotron self-absorbed radio SN model (solid; see Section 6.2), and an off-axis GRB model light curve for a fireball expanding in a constant density ISM (dashed; see Section 6.1), compared with our VLA observations (see Table 3). See text for a discussion of the models and best fit parameters.
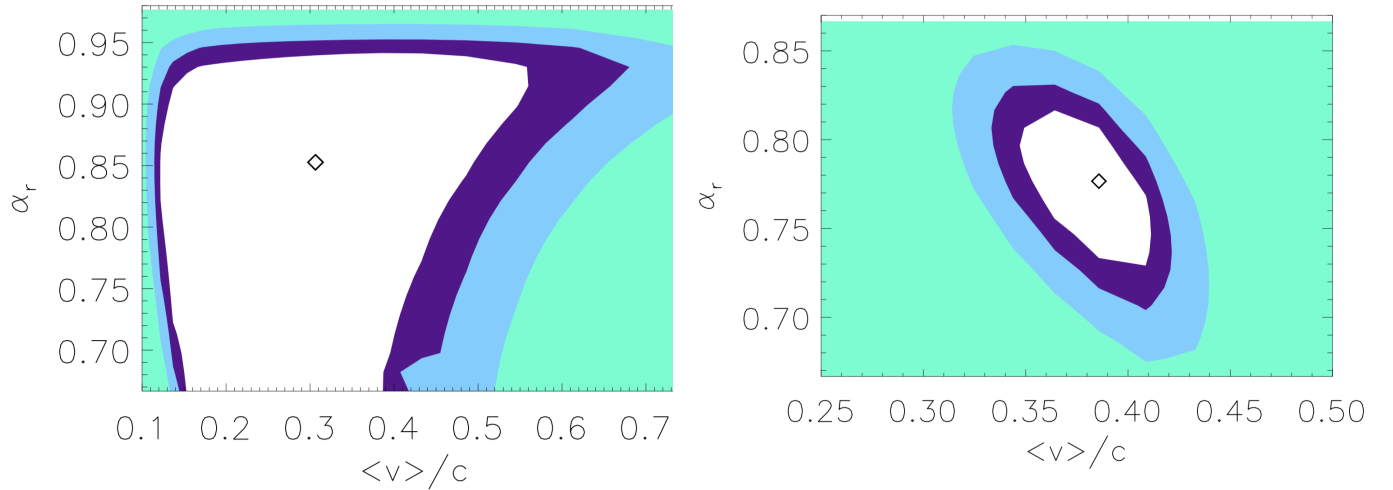

FIG. 9.— PTF11cmh (LEFT) and PTF14dby (RIGHT) best fit results (diamonds) and confidence intervals for the average speed and temporal index of the blastwave radius α_r. We expect $\alpha_r \approx 1$ for an undecelerated explosion, and $\alpha_r \approx 2/3$ for a decelerated explosion in the Sedov-Neumann-Taylor phase (Waxman 2004b). Colors correspond to the following confidence intervals: $\lesssim 68\%$ confidence (white), between 68% and 90% confidence (purple), between 90% and 99% confidence (light blue), and $\gtrsim 99\%$ confidence (aqua green) i.e., contours correspond to $\Delta\chi^2 = 2.3, 4.61, 9.21$ for 2 interesting parameters, respectively. The contours avoid the portions of the parameter space where the model's physical assumptions break down (i.e., the index p of the electron energy distribution reaches its boundary value of $p = 2$).
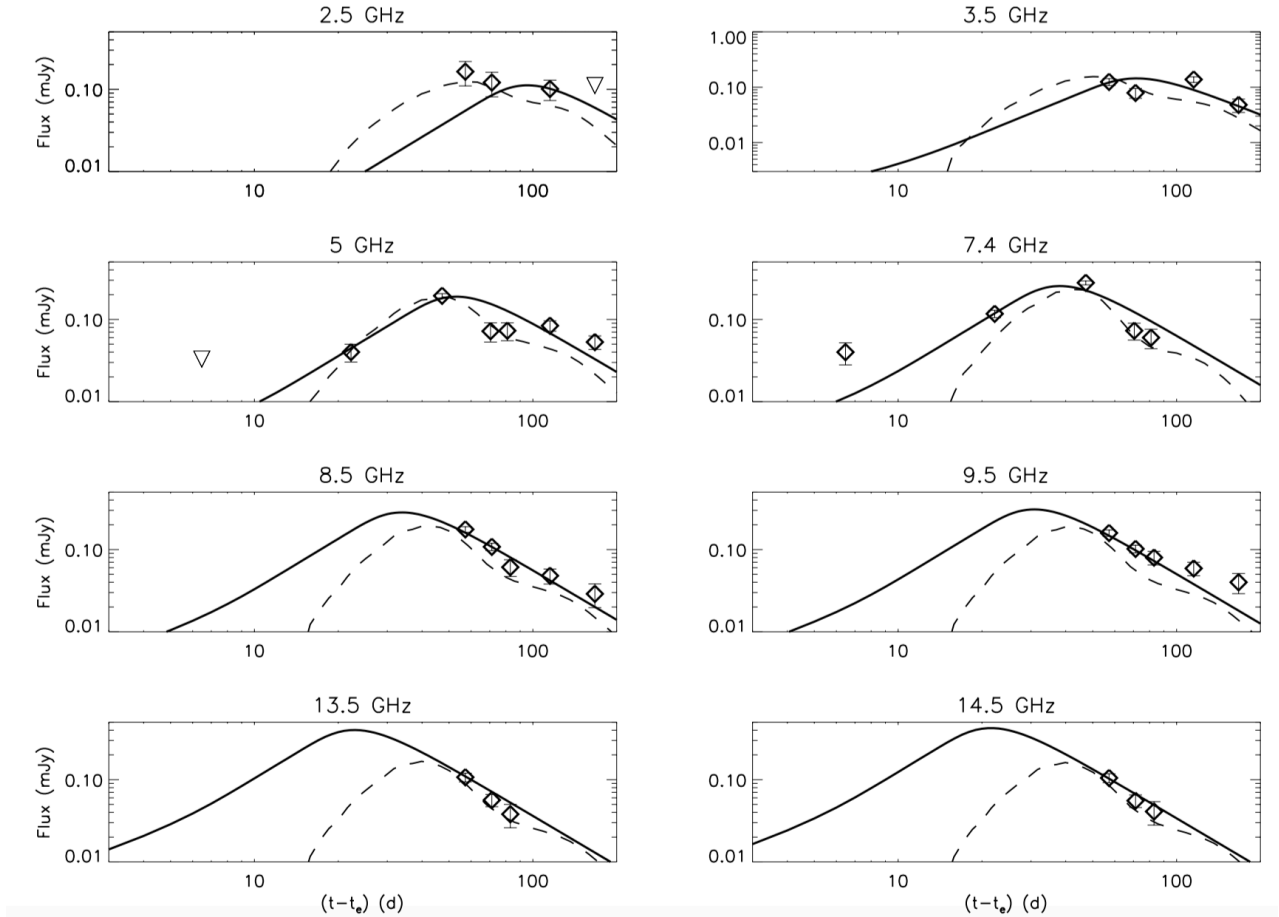
FIG. 10.— Best fit radio light curves of PTF14dby in the synchrotron self-absorbed radio SN model (solid; see Section 6.2), and an off-axis GRB model light curve for a fireball expanding in a constant density ISM (dashed; see Section 6.1), compared with our VLA observations (see Table 3; note that the two data points at $\approx 6\,\mathrm{GHz}$ are not plotted here but have been included in the fit that we use to derive the solid light curves). See text for a discussion of the models and best fit parameters.

with circumstellar medium (CSM). The temporal and spectral evolution of the synchrotron emission is determined by the dynamics, and by the properties of the ejecta and CSM. While young, non-relativistic SNe expand freely (their ejecta are largely un-decelerated), GRB relativistic blast waves expand and decelerate following the BM solution. At late enough times, both non-relativistic radio SNe and GRBs are expected to approach the non-relativistic adiabatic expansion phase (SNT dynamics, see also Section 5). In what follows, we discuss the SNe with radio detections in our sample within these two scenarios (decelerated GRB ejecta and non-relativistic radio SN).

6.1. *GRB jets observed off-axis?*

Three SNe in our sample, PTF11cmh, PTF11qcj, and PTF14dby, were detected during our radio follow-up with the VLA. Interestingly, two out of these three SNe (PTF11qcj and PTF14dby) are found to be spectroscopically similar to SN 1998bw. Thus, the rate of radio detections for the BL-Ic SNe in our sample *spectroscopically* most similar to SN 1998bw is $\approx 2/4 = 50\%$ (see Fig. 2). As noticed in Section 2.3, the X-ray upper-limit on PTF14dby does *not* exclude the presence of X-ray afterglow emission comparable to that of GRB 980425, however its radio emission appears different from SN 1998bw in the fact that it peaks at later times. Moreover, the radio emission from PTF11cmh, PTF11qcj, and PTF14dby is orders of magnitudes dimmer than that of an average long GRB observed on-axis (blue curve shaded are in Fig. 4), and also dimmer than most low-luminosity GRBs with well-sampled radio light curves. Thus, here we address the question of whether the radio emission from these three SNe could be associated with a GRB observed off-axis.

In Figs. 8 and 10 we show a tentative comparison of the observed radio light curves of PTF14dby and PTF11cmh with numerical model light curves of off-axis low-luminosity GRBs expanding in a constant density environment of density $n_{\rm ISM}$ (dashed lines; van Eerten & MacFadyen 2011; van Eerten et al. 2012). We note that numerical models for GRB jets expanding in a wind environment are not currently available to the community (at least not in a format that can allow us to easily compare these models with our observations). Thus, hereafter we limit our discussion to the case of a constant density ISM.

For PTF11cmh (Fig. 8, dashed line), we have set: $\theta_j \approx 10$ deg, observer's angle $\theta_{obs} \approx 90$ deg, beaming corrected energy $E_{51} \approx 0.1$, $n_{\rm ISM} = 10\,{\rm cm}^{-3}$, $\epsilon_B = \epsilon_e \approx 0.1$, and $p \approx 2.2$. These values for the model parameters provide a model light curve in agreement with the (limited) 6 GHz data. We also point out that the limited dataset available for PTF11cmh does leave open the possibility of a mildly-relativistic event (discussed in more detail in the following Section).

For PTF14dby (Fig. 10, dashed line) we have set: $\theta_j \approx 6$ deg, observer's angle $\theta_{obs} \approx 70$ deg, beaming corrected energy $E_{51} \approx 0.01$, $n_{\rm ISM} = 10\,{\rm cm}^{-3}$, $\epsilon_B = \epsilon_e \approx 0.1$, and $p \approx 2.4$. While the simplest off-axis GRB model in a constant density ISM does not provide a perfect match, the model light curves are broadly compatible with the observations of PTF14dby, thus an off-axis GRB cannot be securely ruled out. We also note that in the PTF14dby radio light curve there is a hint for a late-time

peak (or flattening) reminiscent of SN 1998bw, that may be better fitted using off-axis GRB models expanding in a wind environment, and/or by invoking an energy injection episode similar to what has been proposed by Li & Chevalier (1999) for SN 1998bw.

PTF11qcj is the most difficult to interpret within the simplest off-axis GRB models (see also Corsi et al. 2014) due to the clear late-time radio re-brightening. However, this late-time re-brightening requires modifications also to the simplest non-relativistic radio SN model, such as the presence of a denser CSM shell (e.g., Salas et al. 2013).

Based on the tentative comparison with available models described in this Section, and on the results described in Section 5, we can attempt to constrain the fraction of BL-Ic SNe in our sample potentially harboring off-axis GRB jets. Indeed, since $\lesssim 3$ BL-Ic SNe in our sample may be associated with off-axis (low-luminosity) GRBs expanding in an ISM with $n_{\rm ISM} \sim 10\,{\rm cm}^{-3}$ (or $A_* \sim 4$; compare Eqs. (14) and (15) in Waxman 2004b), we set a 99.865% confidence Poisson upper-limit of $\lesssim 12.68/15 \approx 85\%$ on the fraction of BL-Ic SNe possibly harboring off-axis GRBs expanding in media with densities of this order. We note, however, that a comparison with numerical models for off-axis low-luminosity GRBs expanding in a wind environment would be needed to better determine the values of A_* constrained by our dataset.

6.2. *Non-relativistic radio SN emission*

In what follows, we model the radio emission observed from PTF11cmh and PTF14dby within the standard radio SN model based on the interaction of non-relativistic ejecta with CSM deposited via a constant mass-loss rate, constant velocity wind (i.e., $\rho_{\rm CSM} = \dot{M}_w/(4\pi v_w r^2)$) from a massive progenitor (Chevalier 1982). We follow the formulation of this standard model given in Soderberg et al. (2005), which replaces the SNT dynamics with a general parametrization of the shock evolution which enables us to model the early SN synchrotron emission (when the ejecta is very close to free expansion), while recovering (in the appropriate time limit) the correct behavior for GRBs transitioning to the sub-relativistic adiabatic expansion phase (Waxman 2004b).

In the standard model, synchrotron emission observed at time t is produced from an expanding spherical shell of shock-accelerated electrons with radius r and thickness r/η. The shell interacts with a smooth CSM following a self-similar evolution. The electrons, which are accelerated into a power-law energy distribution $N(\gamma) \propto \gamma^{-p}$ (with $\gamma \gtrsim \gamma_m$), carry a fraction ϵ_e of the energy density of the ejecta. Magnetic fields carry a fraction ϵ_B of the energy density. The temporal evolution of the shell and its properties is parametrized as (Soderberg et al. 2005, 2006a):

$$r = r_0 \left(\frac{t-t_e}{t_0}\right)^{\alpha_r} \qquad B = B_0 \left(\frac{t-t_e}{t_0}\right)^{\alpha_B} \qquad (7)$$

$$\gamma_m = \gamma_{m,0} \left(\frac{t-t_e}{t_0}\right)^{\alpha_\gamma} \qquad \frac{\epsilon_e}{\epsilon_B}, = \mathfrak{F}_0 \left(\frac{t-t_e}{t_0}\right)^{\alpha_\mathfrak{F}} . \quad (8)$$

In the above Equations, t_0 is an arbitrary reference time (here set to day 10 since explosion), t_e is the explosion

time of the SN, $\alpha_r = (n-3)/(n-s)$ (Chevalier 1982, 1996) with n the power-law index of the outer SN ejecta density profile ($\rho_{SN} \propto (r/t)^{-n}$), and s the power-law index of the shocked CSM electrons density profile ($n_e \propto r^{-s}$).

Following Chevalier (1996), the magnetic energy density ($U_B \propto B^2$) and the relativistic electron energy density ($U_e \propto n_e \gamma_m$) are assumed to be a fixed fraction (i.e., $\alpha_{\mathfrak{F}} = 0$) of the total post-shock energy density ($U \propto n_e \langle v \rangle^2$, where v is the velocity). Making the additional conservative assumption that the energy of the radio emitting material is partitioned equally into accelerating electrons and amplifying magnetic fields ($\epsilon_e = \epsilon_B$, which implies $\mathfrak{F}_0 = 1$) and assuming $s = 2$ (as expected for a wind density profile), we have (Soderberg et al. 2005, 2006a):

$$U_e \propto U \quad \Rightarrow \alpha_\gamma = 2(\alpha_r - 1), \qquad (9)$$

and

$$U_B \propto U \quad \Rightarrow \alpha_B = \frac{(2-s)}{2}\alpha_r - 1 = -1, \qquad (10)$$

and, for the flux density from the uniform shell of radiating electrons (Soderberg et al. 2005, 2006a):

$$f_\nu = C_f \left(\frac{t-t_e}{t_0}\right)^{(4\alpha_r+1)/2} (1 - \exp(-\tau_\nu))$$
$$\times \left(\frac{\nu}{1\,\mathrm{GHz}}\right)^{5/2} \times F_3(x) F_2^{-1}(x) \,\mathrm{mJy}, \qquad (11)$$

where $C_f = C_f(r_0, B_0, p)$ (see Eq. (A.13) in Soderberg et al. 2005), $x = 2/3(\nu/\nu_m)$, and

$$\nu_m = \gamma_m^2 \frac{eB}{2\pi m_e c} = \gamma_{m,0}^2 \frac{eB_0}{2\pi m_e c} \left(\frac{t-t_e}{t_0}\right)^{2\alpha_\gamma + \alpha_B}$$
$$= \nu_{m,0} \left(\frac{t-t_e}{t_0}\right)^{4\alpha_r - 5} \qquad (12)$$

is the characteristic synchrotron frequency of electrons with Lorentz factor γ_m. As typically assumed for radio SNe, we set $\nu_{m,0} \approx 1\,\mathrm{GHz}$ (which, in turn, implies that $\gamma_{m,0}$ is a function of B_0 only). In Equation (11), F_2 and F_3 are integrals of the modified Bessel function of order 2/3 (see Equation (A11) in Soderberg et al. 2005); and

$$\tau_\nu(t) = C_\tau \left(\frac{t-t_e}{t_0}\right)^{(p-2)\alpha_\gamma + (3+p/2)\alpha_B + \alpha_r}$$
$$\times \left(\frac{\nu}{1\,\mathrm{GHz}}\right)^{-(p+4)/2} F_2(x) =$$
$$C_\tau \left(\frac{t-t_e}{t_0}\right)^{(2p-3)\alpha_r - (5p/2-1)} \left(\frac{\nu}{1\,\mathrm{GHz}}\right)^{-(p+4)/2} F_2(x) \quad (13)$$

is the optical depth (Soderberg et al. 2005, 2006a), with $C_\tau = C_\tau(r_0, B_0, \gamma_{m,0}, p)$ (see Eq. (A.14) in Soderberg et al. 2005). Thus, as evident from Eqs. (11) and (13), the observed spectral and temporal evolutions of the radio emission ultimately depend on the parameters $(r_0, B_0, t_e, p, \alpha_r, \eta)$, which we determine by comparison with the data.

6.2.1. PTF11cmh radio modeling

Our VLA follow-up observations of PTF11cmh started at an epoch of about $\approx 20\,\mathrm{d}$ since optical discovery, and were carried out until more than $10^3\,\mathrm{d}$ after (Table 3). Our first radio detection of PTF11cmh was more than $100\,\mathrm{d}$ since optical discovery.

Because our radio observations for PTF11cmh are very limited, we expect any model fitting to return only tentative estimates of model parameters. Within the standard synchrotron self-absorbed scenario (Section 6.2), we can set $t_e = 55673.336\,\mathrm{MJD}$ (see Table 1) and $\eta = 5$ (as typically assumed in radio SN studies). This leaves 4 free model parameters to be compared with 4 radio detections and 1 upper-limit (see Table 3). We thus attempt a crude fit by considering the upper-limit at epoch $\approx 20\,\mathrm{d}$ since explosion as a data point with flux value equal to the maximum radio flux detected in circular region centered on the optical position of PTF11cmh with radius equal to half the VLA FWHP synthesized beam for the observation, and error equal to the image rms i.e., $15 \pm 24\,\mu\mathrm{Jy}$. This way our fit returns a $\chi^2 \approx 4$ for 1 d.o.f.[21]. From the best fit light curves shown in Fig. 8 (solid lines), we also estimate $\nu_p \approx 5\,\mathrm{GHz}$ at $\approx 100\,\mathrm{d}$ since explosion, and $L_{p,5\,\mathrm{GHz}} \approx 10^{29}\,\mathrm{erg\,s^{-1}\,Hz^{-1}}$. The last is comparable to the radio spectral luminosity of the GRB-associated SN 1998bw (Kulkarni et al. 1998).

The best-fit values for the model parameters are $p \approx 3$, $B_0 \approx 5\,\mathrm{G}$, and a blast-wave radial evolution of $R \approx 9 \times 10^{15}[(t-t_e)/10\,\mathrm{d}]^{0.86}\,\mathrm{cm}$. The last implies an average ejecta speed of $R/\Delta t \approx 0.3\,c$, where c is the speed of light. This is $\approx 3\times$ higher than the average speed of ordinary Ib/c SNe ($\approx 0.1c$), but smaller than relativistic events such as SN 2009bb and SN 1998bw. In Fig. 9 we show the uncertainties on the best values of the average ejecta speed ($\langle v \rangle = r_0/10\,\mathrm{d}$) and power-law index α_r of the temporal evolution of the ejecta radius, as derived by mapping the difference $\Delta\chi^2 = \chi_2^2 - \chi_4^2$, where χ_4^2 is the best fit χ^2 value returned by our 4-parameter fit to the data (see above); and χ_2^2 is the best fit χ^2 value obtained when mapping the α_r-r_0 space over a grid of possible values and minimizing the χ^2 over the remaining two "non-interesting" parameters (e.g, Avni 1976). As evident from this Figure, because of the limited dataset available for this event, the speed of the radio emitting material is very poorly constrained, with the 99% confidence region extending in the range $\langle v \rangle / c \approx 0.11 - 2/3$.

Assuming equipartition ($\epsilon_e = \epsilon_B = 0.33$), and using Eq. (14) in Soderberg et al. (2005), we derive a minimum energy of $E \approx 6 \times 10^{48}(\epsilon_e/0.33)^{-1}[(t-t_e)/10\,\mathrm{d}]^{0.58}\,\mathrm{erg}$ coupled to the fastest radio-emitting outflow. This energy is at the higher end of the range derived for other radio Ib/c SNe (Margutti et al. 2014). However, we also note that because $E \propto r_0^3 \propto \langle v \rangle^3$, a factor of ≈ 6 uncertainty on $\langle v \rangle$ (at 99% confidence) implies a factor of ≈ 200 uncertainty in the estimated ejecta energy.

Finally, the estimated progenitor mass-loss rate is $\dot{M} = 10^{-4}(v_w/1000\,\mathrm{km\,s^{-1}})\,\mathrm{M_\odot\,yr^{-1}}$, where v_w is the velocity of the stellar wind and where we have assumed a nucleon-to-proton ratio of 2 (see Eq. (13) in Soderberg et al. 2005). This mass-loss rate is higher than the typical

---

[21] We do not expect the simplified analytical synchrotron model to provide a perfect fit, and this value of the χ^2 is similar to what obtained in other analyses of radio SN light curves.

range derived for low-luminosity GRBs (see e.g. Fig. 7), and more similar to CSM-interacting BL-Ic SNe such as PTF11qcj (Corsi et al. 2014). Based on these results, we suggest that PTF11cmh is likely a CSM-interacting event similar to PTF 11qcj. However, this conclusion has to be taken with the caveat of being derived from a very limited dataset. Indeed, since $\dot{M} \propto r_0^2 \propto \langle v \rangle^2$, a factor of ≈ 6 uncertainty on $\langle v \rangle$ (at 99% confidence) implies a factor of ≈ 40 uncertainty in the estimated mass-loss rate.

6.2.2. *PTF11qcj radio modeling*

Our VLA follow-up observations of PTF11qcj started about two weeks after optical discovery, and were carried out until $\approx 600\,\mathrm{d}$ after (Corsi et al. 2014). As described in Corsi et al. (2014), modeling our radio observations in the standard synchrotron self-absorbed scenario yielded best-fit values of $B_0 \approx 5.7\,\mathrm{G}$ for the magnetic field, and a blast-wave radial evolution of $R \approx 1.1 \times 10^{16}[(t - t_e)/10\,\mathrm{d}]^{0.80}$ cm (assuming $\eta = 5$). The last implies an average ejecta speed of $R/\Delta t \approx 0.4\,c$. This is $\approx 4\times$ higher than the average speed of ordinary Ib/c SNe ($\approx 0.1c$), but smaller than relativistic events such as SN 2009bb and SN 1998bw. For $\eta = 5$, we also estimated a minimum energy of $E \approx 1.2 \times 10^{49}(\epsilon_e/0.33)^{-1}[(t-t_e)/10\,\mathrm{d}]^{0.4}$ erg coupled to the fastest radio-emitting outflow, and a progenitor mass-loss rate of $\dot{M} \approx 1.5\times10^{-4}(v_w/1000\,\mathrm{km\,s^{-1}})\,\mathrm{M_\odot\,yr^{-1}}$, where v_w is the velocity of the stellar wind (and assuming a nucleon-to-proton ratio of 2).

6.2.3. *PTF14dby radio modeling*

Our VLA follow-up observations of PTF14dby started at an epoch of about $\approx 6\,\mathrm{d}$ since optical discovery, and were carried out until more than $150\,\mathrm{d}$ after (Table 3). The first clear ($\gtrsim 4\sigma$) VLA detection of PTF14dby at $5\,\mathrm{GHz}$ was obtained about $20\,\mathrm{d}$ since optical discovery.

We collected a total of 36 detections and 2 upper-limits for PTF14dby (see Table 3). We model our radio detections in the standard synchrotron self-absorbed scenario (Section 6.2) using a χ^2 minimization procedure where we set $\eta = 5$, so we are left with 5 free model parameters. The fit returns a $\chi^2 \approx 115$ for 31 d.o.f.. From the best fit light curves shown in Fig. 10 (solid lines) we estimate $\nu_p \approx 7.4\,\mathrm{GHz}$ at $\approx 40\,\mathrm{d}$ since explosion, and a spectral peak luminosity of $L_{p,7.4\,\mathrm{GHz}} \approx 3 \times 10^{28}\,\mathrm{erg\,s^{-1}\,Hz^{-1}}$. The last is $\approx 4\times$ smaller than the peak radio luminosity of the GRB-associated SN 1998bw, but comparable to the radio peak luminosity of the engine-drive SN 2009bb (Fig. 5; Soderberg et al. 2010).

The best-fit values for the model parameters are $t_e \approx 56832\,\mathrm{MJD}$ (which is consistent with the discovery date reported in Table 1), $p \approx 2.9$, $B_0 \approx 1.6\,\mathrm{G}$, and a blast-wave radial evolution of $R \approx 9.8 \times 10^{15}[(t - t_e)/10\,\mathrm{d}]^{0.78}$ cm. The last implies an average ejecta speed of $R/\Delta t \approx 0.38\,c$. This is $\approx 4\times$ higher than the average for ordinary Ib/c SNe ($\approx 0.1c$), but smaller than relativistic events such as SN 2009bb and SN 1998bw.

In Fig. 9 we show the uncertainties on the best values of the average ejecta speed ($\langle v \rangle = r_0/10\,\mathrm{d}$) and power-law index α_r obtained in a way similar to what described in the previous Section. As evident from this Figure,

the 99% confidence region for the average ejecta speed is $\langle v \rangle / c \approx 0.32 - 0.44$.

Assuming equipartition ($\epsilon_e = \epsilon_B = 0.33$), we derive a minimum energy of $E \approx 8 \times 10^{47}(\epsilon_e/0.33)^{-1}[(t - t_e)/10\,\mathrm{d}]^{0.34}$ erg coupled to the fastest radio-emitting outflow.

Finally, the estimated progenitor mass-loss rate is $\dot{M} \approx 5 \times 10^{-6}(v_w/1000\,\mathrm{km\,s^{-1}})\,\mathrm{M_\odot\,yr^{-1}}$ (where again we have assumed a nucleon-to-proton ratio of 2). This mass-loss rate is in agreement with values derived for low-luminosity GRBs (see e.g. Fig. 7), and smaller that the one derived for CSM-interacting BL-Ic SNe such as PTF11qcj ($\dot{M} \approx 10^{-4}(v_w/1000\,\mathrm{km\,s^{-1}})\,\mathrm{M_\odot\,yr^{-1}}$; Corsi et al. 2014). This, together with the fact that the simplest off-axis GRB models (dashed lines in Fig. 10) are in broad agreement with the radio light curve of PTF14dby, calls for a more accurate numerical modeling of this SN which is beyond the scope of this paper, but that we hope will get the attention of the community.

7. SUMMARY AND CONCLUSION

We have presented the P48 photometry, spectral classification, and radio/X-ray follow-up observations of 15 BL-Ic SNe discovered by the PTF/iPTF. All of the SNe in our sample exclude radio afterglows typical of long duration GRBs at cosmological distances observed on-axis. Thanks to deep VLA follow-up observations, we are able to exclude the presence of 1998bw-like (or 2009bb-like) radio emission for most of the SNe in our sample. Because radio emission traces the fastest moving ejecta, we conclude that events as relativistic as, and observationally similar to, SN 1998bw are $\lesssim 41\%$ of the BL-Ic population (99.865% confidence). None of our upper-limits exclude radio emission similar to the radio afterglow of GRB 060218, which faded on timescales much faster than our VLA monitoring campaign was designed to target.

Using the X-ray upper-limits collected via our programs, we rule out the presence of off-axis GRB jets observed slightly off-axis for some of the SNe in our sample. We also constrain the energy and density parameters of (largely) off-axis GRBs potentially harbored by the SNe in our sample for which 1998bw-like radio emission was excluded. While we can rule out the presence of GRBs as energetic as GRB 030329 observed at large off-axis angles and expanding in a constant ISM with density $n_{0,ISM} \gtrsim 0.1$, we cannot rule out the presence of off-axis GRBs expanding in a low-density wind medium, such as the one found around GRB 130427A.

Finally, we presented the detailed radio modeling of two radio-loud BL-Ic, PTF11cmh and PTF14dby, which add to our previous radio detection of PTF11qcj. While the ejecta speed of PTF11cmh is very poorly constrained due to the limited dataset, we constrained the speed of the radio emitting material in PTF14dby to be intermediate between that of non-relativistic BL-Ic SNe, and relativistic events such as SN 2009bb. Because we cannot securely rule out off-axis GRB models for these three events, we set an upper-limit of $\lesssim 85\%$ (99.865% confidence) on the fraction of BL-Ic SNe in our sample that could potentially harbor a GRB observed off-axis and expanding in a medium of density $n_{ISM} \sim 10\,\mathrm{cm^{-3}}$. This estimate could be improved by comparing our data with numerical models for off-axis GRBs expanding in a wind

medium.

In summary, our results show that the VLA (thanks to its improved sensitivity) working in tandem with surveys like the iPTF, can help us clarify key open questions regarding the GRB-SN connection (such as, what fraction of purely BL-Ic SNe can host low-luminosity GRBs) and enable us to discover more events on the dividing line between ordinary BL-Ic and relativistic GRBs. Over the course of 5 years, we have greatly enlarged the sample of BL-Ic SNe (discovered independently of a GRB trigger) with radio follow-up within one year since discovery. We expect that the Zwicky Transient Factory will be able to boost even further the rate at which we are discovering the rare BL-Ic events (Smith et al. 2014).

REFERENCES

Armstrong, M., et al. 2002, IAUC, 7845

Avni, Y. 1976, ApJ, 210, 642

Bennett, C. L., Larson, D., Weiland, J. L., & Hinshaw, G. 2014, ApJ, 794, 135

Berger, E., Kulkarni, S. R., Frail, D. A., & Soderberg, A. M. 2003a, Astrophys. J., 599, 408

Berger, E., et al. 2003b, Nature, 426, 154

Berger, E., et al. 2003c, Nature, 426, 154

Bietenholz, M. F., De Colle, F., Granot, J., Bartel, N., & Soderberg, A. M. 2014, MNRAS, 440, 821

Branch, D. 1999, ArXiv Astrophysics e-prints, astro-ph/9906168

Burrows, D. N., et al. 2005, Space Sci. Rev., 120, 165

Chakraborti, S., et al. 2015, ApJ, 805, 187

Chandra, P., & Frail, D. A. 2012, ApJ, 746, 156

Chevalier, R. A. 1982, Astrophys. J., 259, 302

Chevalier, R. A. 1996, in Astronomical Society of the Pacific Conference Series, Vol. 93, Radio Emission from the Stars and the Sun, ed. A. R. Taylor & J. M. Paredes, 125

Chomiuk, L., & Soderberg, A. 2010, The Astronomer's Telegram, 2483, 1

Clocchiatti, A., Suntzeff, N. B., Covarrubias, R., & Candia, P. 2011, AJ, 141, 163

Corsi, A., et al. 2011, Atrophys. J., 741, 76

Corsi, A., et al. 2014, ApJ, 782, 42

Drake, A. J., et al. 2009, ApJ, 696, 870

Drake, A. J., et al. 2013, The Astronomer's Telegram, 4984, 1

Frail, D. A., et al. 2001, ApJ, 562, L55

Frail, D. A., Soderberg, A. M., Kulkarni, S. R., Berger, E., Yost, S., Fox, D. W., & Harrison, F. A. 2005, ApJ, 619, 994

Gal-Yam, A., et al. 2010, The Astronomer's Telegram, 2817, 1

Gal-Yam, A., et al. 2006, ApJ, 639, 331

Gal-Yam, A., Ofek, E. O., & Shemmer, O. 2002, Mon. Not. Roy. Astr. Soc., 332, L73

Galama, T. J., et al. 1998, Nature, 395, 670

Garmire, G. P., Bautz, M. W., Ford, P. G., Nousek, J. A., & Ricker, G. R., Jr. 2003, in Society of Photo-Optical Instrumentation Engineers (SPIE) Conference Series, Vol. 4851, X-Ray and Gamma-Ray Telescopes and Instruments for Astronomy., ed. J. E. Truemper & H. D. Tananbaum, 28

Gehrels, N., et al. 2004, Astrophys. J., 611, 1005

Ghirlanda, G., et al. 2013, Mon. Not. Roy. Astr. Soc., 428, 1410

Graham, J. F., & Fruchter, A. S. 2013, ApJ, 774, 119

Graham, J. F., & Schady, P. 2015, ArXiv e-prints 1511.01466

Granot, J., & Loeb, A. 2003, Astrophys. J. Lett., 593, L81

Granot, J., Panaitescu, A., Kumar, P., & Woosley, S. E. 2002, Astrophys. J. Lett., 570, L61

Guetta, D., & Della Valle, M. 2007, ApJL, 657, L73

Hadjiyska, E., et al. 2012, in IAU Symposium, Vol. 285, IAU Symposium, ed. E. Griffin, R. Hanisch, & R. Seaman, 324

Hjorth, J., et al. 2012, ApJ, 756, 187

Iwamoto, K., et al. 1998, ArXiv Astrophysics e-prints

Kalberla, P. M. W., Burton, W. B., Hartmann, D., Arnal, E. M., Bajaja, E., Morras, R., & Pöppel, W. G. L. 2005, A&A, 440, 775

Kamble, A., & Soderberg, A. 2013, The Astronomer's Telegram, 4997, 1

Kasliwal, M. M., & Cenko, S. B. 2010, The Astronomer's Telegram, 2471, 1

Kelly, P. L., Filippenko, A. V., Modjaz, M., & Kocevski, D. 2014, ApJ, 789, 23

Krühler, T., et al. 2015, A&A, 581, A125

Kulkarni, S. R., et al. 1998, Nature, 395, 663

Laher, R. R., et al. 2014, PASP, 126, 674

Law, N. M., et al. 2009, Pub. of the Astron. Soc. of the Pacific, 121, 1395

Levesque, E. M., Kewley, L. J., Berger, E., & Zahid, H. J. 2010, AJ, 140, 1557

Levinson, A., et al. 2002, Astrophys. J., 576, 923

Li, Z.-Y., & Chevalier, R. A. 1999, ApJ, 526, 716

Liang, E., Zhang, B., Virgili, F., & Dai, Z. G. 2007, ApJ, 662, 1111

Liang, E.-W., Racusin, J. L., Zhang, B., Zhang, B.-B., & Burrows, D. N. 2008, ApJ, 675, 528

Livio, M., & Waxman, E. 2000, ApJ, 538, 187

Maguire, K., et al. 2012, Mon. Not. Roy. Astr. Soc., 426, 2359

Margutti, R., et al. 2014, ApJ, 797, 107

Margutti, R., et al. 2013, The Astrophysical Journal, 778, 18

Mazzali, P. A., et al. 2002, Astrophys. J. Lett., 572, L61

Mazzali, P. A., Iwamoto, K., & Nomoto, K. 2000, Astrophys. J., 545, 407

Mazzali, P. A., et al. 2005, Science, 308, 1284

Melandri, A., et al. 2014, A&A, 567, A29

Mészáros, P. 2006, Reports on Progress in Physics, 69, 2259

Milisavljevic, D., et al. 2015, ApJ, 799, 51

Miller, J. S., & Stone, R. 1993, Lick Ob. Tech. Rep. 66

Modjaz, M., et al. 2008, AJ, 135, 1136

Nakar, E., Piran, T., & Granot, J. 2002, Astrophys. J., 579, 699

Ofek, E. O., et al. 2007, ApJ, 662, 1129

Ofek, E. O., Frail, D. A., Breslauer, B., Kulkarni, S. R., Chandra, P., Gal-Yam, A., Kasliwal, M. M., & Gehrels, N. 2011, Astrophys. J., 740, 65

Ofek, E. O., et al. 2012, Pub. of the Astron. Soc. of the Pacific, 124, 62

Ofek, E. O., et al. 2013, Nature, 494, 65

Oke, J. B., et al. 1995, PASP, 107, 375

Oke, J. B., & Gunn, J. E. 1982, Pub. of the Astron. Soc. of the Pacific, 94, 586

Paczynski, B. 2001, Acta Astronomica, 51, 1

Pandey, S. B., Anupama, G. C., Sagar, R., Bhattacharya, D., Sahu, D. K., & Pandey, J. C. 2003, MNRAS, 340, 375

Patat, F., et al. 2001, Astrophys. J., 555, 900

Perley, D. A., et al. 2014, ApJ, 781, 37

Perley, D. A., et al. 2015, ArXiv e-prints arXiv150402482P

Perley, D. A., et al. 2013, ApJ, 778, 128

Perley, R., et al. 2009, IEEE Proceedings, 97, 1448

Pignata, G., et al. 2011, Astrophys. J., 728, 14

Piran, T. 2004, Reviews of Modern Physics, 76, 1143

Podsiadlowski, P., Mazzali, P. A., Nomoto, K., Lazzati, D., & Cappellaro, E. 2004, ApJ, 607, L17

Prentice, S. J., et al. 2016, MNRAS, 458, 2973

Racusin, J. L., et al. 2009, ApJ, 698, 43

Ramirez-Ruiz, E., Granot, J., Kouveliotou, C., Woosley, S. E., Patel, S. K., & Mazzali, P. A. 2005, ApJ, 625, L91

Rau, A., et al. 2009, Pub. of the Astron. Soc. of the Pacific, 121, 1334

Rhoads, J. E. 1999, Astrophys. J., 525, 737

Rhoads, J. E. 2003, ApJ, 591, 1097

Salas, P., Bauer, F. E., Stockdale, C., & Prieto, J. L. 2013, Mon. Not. Roy. Astr. Soc., 428, 1207

Santana, R., Barniol Duran, R., & Kumar, P. 2014, ApJ, 785, 29

Schlafly, E. F., & Finkbeiner, D. P. 2011, Astrophys. J., 737, 103

Singer, L. P., et al. 2015, ApJ, 806, 52

Smartt, S. J., et al. 2015, A&A, 579, A40

Smith, R. M., et al. 2014, in Society of Photo-Optical Instrumentation Engineers (SPIE) Conference Series, Vol. 9147, Society of Photo-Optical Instrumentation Engineers (SPIE) Conference Series, 79

Soderberg, A., & Chomiuk, L. 2011, The Astronomer's Telegram, 3101, 1

Soderberg, A. M., et al. 2010, Nature, 463, 513

Soderberg, A. M., Chevalier, R. A., Kulkarni, S. R., & Frail, D. A. 2006a, Astrophys. J., 651, 1005

Soderberg, A. M., Kulkarni, S. R., Berger, E., Chevalier, R. A., Frail, D. A., Fox, D. B., & Walker, R. C. 2005, Astrophys. J., 621, 908

Soderberg, A. M., et al. 2004, Nature, 430, 648

Soderberg, A. M., et al. 2006b, Nature, 442, 1014

Soderberg, A. M., Nakar, E., Berger, E., & Kulkarni, S. R. 2006c, Astrophys. J., 638, 930

Stanek, K. Z., et al. 2003, ApJ, 591, L17

Taubenberger, S., et al. 2006, Mon. Not. Roy. Astr. Soc., 371, 1459

Tomasella, L., Benetti, S., Pastorello, A., Cappellaro, E., Turatto, M., & Ochner, P. 2013, The Astronomer's Telegram, 4989, 1

Valenti, S., et al. 2008, Mon. Not. Roy. Astr. Soc., 383, 1485

van Eerten, H., van der Horst, A., & MacFadyen, A. 2012, ApJ, 749, 44

van Eerten, H. J., & MacFadyen, A. I. 2011, Astrophys. J.L, 733, L37

van Eerten, H. J., & MacFadyen, A. I. 2012, ApJ, 751, 155

Walker, E. S., et al. 2014, MNRAS, 442, 2768

Waxman, E. 2004a, ApJ, 605, L97

Waxman, E. 2004b, ApJ, 602, 886

Weiler, K. W., Sramek, R. A., Panagia, N., van der Hulst, J. M., & Salvati, M. 1986, Astrophys. J., 301, 790

Woosley, S. E., & Bloom, J. S. 2006, Ann. Rev. Astron. Astrophys., 44, 507

Wright, E. L. 2006, PASP, 118, 1711

Xu, D., et al. 2013, ApJ, 776, 98

Yaron, O., & Gal-Yam, A. 2012, Pub. of the Astron. Soc. of the Pacific, 124, 668

York, D. G., et al. 2000, The Astronomical Journal, 120, 1579

Zhang, B.-B., van Eerten, H., Burrows, D. N., Ryan, G. S., Evans, P. A., Racusin, J. L., Troja, E., & MacFadyen, A. 2015, ApJ, 806, 15

Zhang, W., & MacFadyen, A. 2009, ApJ, 698, 1261

TABLE 3 VLA observations. For non-detections, the quoted UL are at 3σ
(where σ is the image rms) unless otherwise stated.

PTF Name	T_{VLA}[j] (MJD)	ΔT_{VLA}[k] (d)	Conf.	ν (GHz)	BW (MHz)	Flux (μJy)	Reference
10bzf	55268.222	18	D	5.0	256	$\lesssim 33$	Chomiuk & Soderberg (2010)
”	55337.221	87	D	6.0	1024	$\lesssim 36$	Corsi et al. (2011)
”	55527.490	277	C	5.0	256	$\lesssim 35$	Corsi et al. (2011)
10qts	55426.028	13	D	8.5	256	$\lesssim 86$	Gal-Yam et al. (2010)
”	55948.524	535	DnC	6.2	2048	$\lesssim 39$	This paper
”	55950.435	537	DnC	6.2	2048	$\lesssim 28$	This paper
10xem	55767.647	297	A	5.0	256	$\lesssim 66$	This paper
10aavz	55566.527	52	C	4.9	256	$\lesssim 31$	Soderberg & Chomiuk (2011)
”	55770.969	256	A	4.9	256	$\lesssim 105$	This paper
11cmh	55692.145	19	B	8.4	256	$\lesssim 72$	This paper
”	55949.356	276	DnC	6.3	2048	159 ± 11	This paper
”	56766.099	1093	A	6.2	2048	17.4 ± 5.4	This paper
”	56781.411	1108	”	1.7	”	57 ± 13	This paper
”	56808.981	1136	”	2.9	”	18.0 ± 4.2	This paper
11img	55781.981	31	A	5.0	256	$\lesssim 48$	This paper
”	55950.478	199	DnC	5.0	2048	$\lesssim 66$	This paper
11lbm	55812.283	19	A	5.0	256	$\lesssim 78$	This paper
”	55948.043	155	DnC	6.2	2048	$\lesssim 28$	This paper
12as	55933.555	8	DnC	6.2	2048	$\lesssim 87$	This paper
”	55947.382	22	DnC	6.2	2048	$\lesssim 69$	This paper
”	56999.567	1074	C	6.2	2048	$\lesssim 75$[22]	This paper
13u	56391.376	67	D	6.2	2048	$\lesssim 95$[23]	This paper
”	56767.366	443	A	6.2	2048	$\lesssim 14$	This paper
”	57311.028	987	D	6.2	2048	$\lesssim 100$[24]	This paper
13alq	56401.120	7	D	4.8	2048	$\lesssim 30$	Kamble & Soderberg (2013)
13alq	56423.080	29	DnC	6.2	2048	$\lesssim 60$[25]	This paper
13alq	57336.833	942	D	6.3	2048	$\lesssim 33$	This paper
13ebw	56667.566	46	B	6.2	2048	$\lesssim 15$	This paper
”	57001.417	380	C	6.2	2048	$\lesssim 41$[26]	This paper
14dby	56838.197	6	D	5.2	1024	$\lesssim 33$	This paper
”	”	”	”	7.5	”	40 ± 12	”
”	56853.994	22	”	5.2	”	40.1 ± 9.8	”
”	”	”	”	7.5	”	117 ± 12	”
”	56879.117	47	”	5.0	”	194 ± 12	”
”	”	”	”	7.4	”	279 ± 15	”
”	56889.108	57	”	2.5	”	164 ± 54	”
”	”	”	”	3.3	”	125 ± 18	”
”	”	”	”	8.5	”	176 ± 14	”
”	”	”	”	9.5	”	159 ± 14	”
”	”	”	”	13.5	”	107 ± 13	”
”	”	”	”	14.5	”	105 ± 13	”
”	56902.138	70	”	5.0	”	72 ± 19	”
”	”	”	”	7.4	”	73 ± 17	”
”	56903.045	71	”	2.7	”	121 ± 40	”
”	”	”	”	3.2	”	79 ± 16	”
”	”	”	”	8.5	”	108 ± 11	”
”	”	”	”	9.5	”	102 ± 11	”
”	”	”	”	13.5	”	56.5 ± 9.6	”
”	”	”	”	14.5	”	55.5 ± 9.7	”
”	56913.144	81	”	5.1	”	73 ± 18	”
”	”	”	”	7.5	”	60 ± 16	”
”	56914.770	83	”	8.5	”	61 ± 14	”
”	”	”	”	9.5	”	80 ± 15	”
”	”	”	”	13.5	”	38 ± 12	”
”	”	”	”	14.5	”	41 ± 13	”
”	56946.949	115	DnC	2.5	”	101 ± 28	”
”	”	”	”	3.5	”	138 ± 16	”
”	”	”	”	5.0	”	84 ± 12	”
”	”	”	”	6.0	”	79 ± 15	”
”	”	”	”	8.5	”	48 ± 10	”
”	”	”	”	9.5	”	59 ± 11	”
”	56998.800	167	C	2.5	”	$\lesssim 111$	”
”	”	”	”	3.4	”	48 ± 13	”
”	”	”	”	5.0	”	53 ± 10	”
”	”	”	”	6.0	”	44 ± 14	”
”	”	”	”	8.5	”	28.9 ± 9.3	”
”	”	”	”	9.5	”	40 ± 11	”
PTF14gaq	56932.496	8	DnC	6.3	2048	$\lesssim 28$	This paper
”	56998.857	75	C	6.2	2048	$\lesssim 25$	This paper
”	57335.919	411	D	6.3	2048	$\lesssim 19$	This paper

[22] 5σ UL corresponding to the brightness of the host galaxy.
[23] 10σ UL corresponding to the brightness of the host galaxy.
[24] 10σ UL corresponding to the brightness of the host galaxy.

[25] 3.6σ UL.
[26] 7σ UL corresponding to the brightness of the host galaxy.

TABLE 3 VLA observations. For non-detections, the quoted UL are at 3σ
(where σ is the image rms) unless otherwise stated.

PTF Name	$T_{\rm VLA}$[j] (MJD)	$\Delta T_{\rm VLA}$[k] (d)	Conf.	ν (GHz)	BW (MHz)	Flux (μJy)	Reference
PTF15dld	57336.049	18	D	5.0	2048	$\lesssim 110$[27]	This paper

[j] The VLA observation time $T_{\rm VLA}$ is the time at the mid-point of the VLA observation.

[k] VLA observation epoch in days since PTF discovery, not corrected for redshift effects.

[27] 10σ UL corresponding to the brightness of the host galaxy.